ANNUAL REPORT

Department of Meteorology
The University of Wisconsin
Madison, Wisconsin

December, 1966

A Physical-Numerical Model for Inferring Tropospheric Structure from Satellite Radiation Measurements

William L. Smith

Note on the Relationship Between Total Perciptable Water and Surface Dew Point

William L. Smith

The Contribution of Infrared Cooling to the Vertical Motion Field and its Implication in Atmospheric Energetics

Ben R. Bullock Lyle H. Horn Donald R. Johnson

The research reported in this document has been supported by the National Environmental Satellite Center of the Environmental Science Services. Administration under grant WBG 52.

ANNUAL REPORT

Department of Meteorology
The University of Wisconsin
Madison, Wisconsin

December, 1966

A Physical-Numerical Model for Inferring Tropospheric Structure from Satellite Radiation Measurements

William L. Smith

Note on the Relationship Between Total Perciptable Water and Surface Dew Point

William L. Smith

The Contribution of Infrared Cooling to the Vertical Motion Field and its Implication in Atmospheric Energetics

Ben R. Bullock Lyle H. Horn Donald R. Johnson

The research reported in this document has been supported by the National Environmental Satellite Center of the Environmental Science Services. Administration under grant WBG 5L.

General Introduction

The research presented here in the form of an annual report consists of three studies which have been supported by United States Weather Bureau Grant WBG 52.

The studies presented in this year's report are primarily concerned with 1) an investigation of an inference technique that may play an important role in obtaining data necessary for global analysis and large-scale energetics studies, and 2) with the evaluation of a method that is currently employed in many energy conversion investigations. The method suggested by Smith to infer vertical temperature and moisture profiles from infrared radiation measurements made from a satellite may eventually lead to a global coverage of atmospheric temperature and moisture data. This information combined with satellite measurements of the amount of energy entering and leaving the earth-atmosphere system is a prerequisite to an adequate understanding of atmospheric energetics.

The study by Bullock, Horn, and Johnson involving contribution of infrared radiation processes to the vertical motion field points out some of the limitations of using the adiabatic method to obtain vertical motion. The results of the study imply that the neglect of non-adiabatic processes in evaluating vertical motions may lead to significant underestimations of the conversion of available potential energy to kinetic energy.

Lyle H. Horn
Donald R. Johnson
Joint Principal Investigators

Madison, Wisconsin
December 1966

400-87

A Physical-Numerical Model for Inferring Tropospheric Structure from Satellite Radiation Measurements

William Leo Smith

ABSTRACT:

A numerical model based on physical considerations is developed which utilizes a set of five radiation measurements over relatively broad spectral intervals (20 cm^{-1} to 40 cm^{-1}) to deduce: (1) surface temperature; (2) lapse rate in the lowest 50 mb; (3) lapse rate above the lowest 50 mb; (4) surface water vapor mixing ratio; and (5) the lapse of moisture with height. Simulated trials indicate that the inferred profiles of temperature and moisture are sufficient to describe the basic qualities of the troposphere from the surface to about 300 mb. The average root mean square temperature errors inherent in the physical modeling are about 2°C. The restraints imposed by the physical modeling are within the resolution of ordinary synoptic analysis of constant pressure level height and moisture fields.

The solutions obtained by the model are shown to be relatively insensitive to random instrumental errors of the magnitude expected to be inherent in the necessary satellite measurements. The resulting rms errors in the deduced temperature profiles are in general about the same magnitude as those inherent in the physical modeling. The effect of instrumental noise on the deduced moisture profiles is more severe resulting in relative errors of about 20 percent. It is anticipated that errors resulting from undetected aerosol and thin cloud layers or errors made in estimating cloud heights and amounts will impose far greater uncertainties in the inferred profiles than the errors resulting from instrumental noise.

1. INTRODUCTION

Since the inception of the meteorological satellite, much attention has been directed toward the problem of inferring the temperature structure of the atmosphere from infrared radiation observations taken from oribiting vehicles. Unfortunately, no unique closed form solution for the temperature profile can be obtained from a finite number of remote radiation measurements. Nevertheless, numerous approximate solutions based on inversion techniques which in theory give reasonable approximations to the true solution may be found in the literature (Wark, 1961; Yamamoto, 1961; King, 1964, and others). However, when realistic data possessing random instrumental errors are utilized, severe stability problems are encountered by most inverse techniques. Wark and Fleming (1966) have overcome much of the instability encountered in the inference of stratospheric temperature by utilizing empirical orthogonal functions generated from climatological data. All inverse solutions, however, become extremely complex for the lower eight-tenths of the atmospheric mass due to the presence of clouds, water vapor, and particulates.

In this paper a numerical model has been developed which makes use of a finite number of remote radiant observations in relatively wide spectral intervals to deduce the temperature and moisture structure of the troposphere. The physical nature of the model is adequate to describe the significant qualities of the troposphere and yet be relatively insensitive to random instrumental errors of the magnitude which might be encountered on a real-time basis.

2. RADIATION INTENSITY SENSED BY A SATELLITE

The infrared irradiance sensed by a satellite-borne radiometer is a function of the temperature profile and optical properties of the atmosphere. Due to the altitude of a satellite, the irradiance measured, even through a narrow cone, represents an integral value of the outgoing radiant intensities over a cross-sectional area of several square kilometers. Although the vertical profiles of temperature and absorbing gas may generally be considered horizontally uniform over the area viewed, in many instances the cloud characteristics cannot be considered uniform. However, if the aperture angle ϕ of the sensing cone is sufficiently small, then the relation between the satellite-measured irradiance, $F_S(\nu)$, at the frequency ν and the integral value of the radiant intensities illuminating the sensing surface may be reduced to:

$$F_S(\nu) = \bar{I}(\nu)\pi \, \mathrm{Sin}^2 \frac{\phi}{2} \qquad (1)$$

where $\bar{I}(\nu)$ represents the average value of the radiant intensities sensed by the satellite. Letting N denote the percentage of cloud cover within the field of view weighted according to the geometric and angular characteristics of the satellite, the average radiant intensity of infrared radiation sensed through the cone is:

$$\bar{I}(\nu) = N\,\bar{I}_{cd}(\nu) + (1-N)\,\bar{I}_{cl}(\nu) \tag{2}$$

where $\bar{I}_{cd}(\nu)$ and $\bar{I}_{cl}(\nu)$ represent the average values of the radiance leaving atmospheric columns containing clouds and clear of clouds, respectively. The infrared radiance leaving the clear columns is governed by the transfer equation (Chandrasekhar, 1950):

$$I_{cl}(\nu) = \xi(\nu, p_0)B[\nu, T(p_0)]\tau[\nu, u(p_0)] - \int_0^{p_0} B[\nu, T(p)]\,\frac{\partial\tau[\nu, u(p)]}{\partial p}\,dp \tag{3}$$

where $\xi(\nu, p_0)$ is the emissivity of the earth's surface, $B[\nu, T(p)]$ is the Planck radiance, $\tau[\nu, u(p)]$ is the transmissivity of the total optically active gas, u, (specifically CO_2 and/or water vapor) extending from the pressure level p to the top of the atmosphere, and p_0 refers to the pressure at the earth's surface. It should be noted that τ is also slightly dependent on the temperature of the gas. The total absorbing gas between any two pressure levels p_1 and p_2 can be written under the assumption of hydrostatic equilibrium as:

$$u = \frac{1}{g}\int_{p_1}^{p_2} q(p)dp \tag{4}$$

where $q(p)$ is the mixing ratio of the gas at the pressure p and g is the gravitational acceleration.

An expression similar to (3) may be written for the intensity of the radiation leaving cloudy atmospheric columns:

$$I_{cd}(\nu) = I(\nu, p_c)\tau[\nu, u(p_c)] - \int_0^{p_c} B[\nu, T(p)]\,\frac{\partial\tau[\nu, u(p)]}{\partial p}\,dp \tag{5}$$

where $I(\nu, p_c)$ is the upward intensity at the pressure p_c just above the highest cloud in the column. Due to the scattering effects of cloud droplets, the exact expression for $I(\nu, p_c)$ may be solved only if the drop size distribution and concentration within the cloud and cloud thickness is well known. Since this information is not easily accessible, especially from satellite observations, the exact expression must be replaced by one which utilizes a parameter, related to the cloud type, which adequately accounts for the resultant changes in the upward stream due to the presence of clouds. The resultant

change of the upward radiance may be described by considering the vertical extent of the clouds to be an infinitesimal slab centered at a pressure level p_c and having an associated slab (cloud) temperature T_c. The emission of the cloud may then be given by $\xi(\nu, p_c)B[\nu, T(p_c)]$ where $\xi(\nu, p_c)$ is the slab emissivity of the cloud which is defined as the ratio of the true cloud emission to the Planck emission at the temperature T_c. The transmission through the cloud layer may then be described by a slab transmissivity $\tau_c(\nu)$ given by:

$$\tau_c(\nu, p_c) = \frac{I(\nu, p_c) - \xi(\nu, p_c)B[\nu, T(p_c)]}{\xi(\nu, p_o)B[\nu, T(p_o)]\tau[\nu, u(p_c - p_o)] - \int_{p_c}^{p_o} B[\nu, T(p)] \frac{\partial \tau[\nu, u(p_c - p)]}{\partial p} dp} \tag{6}$$

where the denominator represents the upward intensity of radiation just below the cloud, and $\tau[\nu, u(p_c - p)]$ is the transmissivity of the gas between the level p and the cloud pressure level p_c. Assuming the slab faces to be non-reflecting in the infrared, then $\xi(\nu, p_c) = 1 - \tau(\nu, p_c)$ and it follows from (6) that:

$$I(\nu, p_c) = \xi(\nu, p_c)B[\nu, T(p_c)] + [1 - \xi(\nu, p_c)] \left\{ \xi(\nu, p_o)B[\nu, T(p_o)] \cdot \tau[\nu, u(p_c - p_o)] - \int_{p_c}^{p_o} B[\nu, T(p)] \frac{\partial \tau[\nu, u(p_c - p)]}{\partial p} dp \right\} \tag{7}$$

The intensity of radiation leaving the cloudy atmospheric columns may be obtained by substituting (7) into (5) to yield:

$$I_{cd}(\nu) = \xi(\nu, p_c)B[\nu, T(p_c)]\tau[\nu, u(p_c)] - \int_0^{p_c} B[\nu, T(p)] \frac{\partial \tau[\nu, u(p)]}{\partial p} dp + \tau[\nu, u(p_c)][1 - \xi(\nu, p_c)] \left\{ \xi[\nu, T(p_o)]\tau[\nu, u(p_c - p_o)]B[\nu, T(p_o)] - \int_{p_c}^{p_o} B[\nu, T(p)] \frac{\partial \tau[\nu, u(p_c - p)]}{\partial p} dp \right\} \tag{8}$$

Assuming that (3) and (8) pertain to the average temperature, moisture, and cloud conditions within the area viewed, they may be substituted into (2) and simplified to yield the following expression for the average intensity of radiation sensed by a satellite:

$$\bar{I}(\nu) = \xi^*(\nu, p_c)B[\nu, T(p_c)]\tau[\nu, u(p_c)] - \int_0^{p_c} B(\nu, T(p)) \frac{\partial \tau[\nu, u(p)]}{\partial p} dp$$
$$+ [1 - \xi^*(\nu, p_c)]\left\{\xi[\nu, T(p_o)]B[\nu, T(p_o)]\tau[\nu, u(p_o)]\right.$$
$$\left. - \int_{p_c}^{p_o} B[\nu, T(p)] \frac{\partial \tau[\nu, u(p)]}{\partial p} dp \right\} \qquad (9)$$

where $\xi^*(\nu, p_c)$, hereafter referred to as the effective emissivity, is the product of the cloud slab emissivity and the percentage of cloud cover within the field of view of the radiometer. It is noted that the effective emissivity pertaining to a relatively large viewing area (say $50 km^2$) might be obtained from High Resolution Infrared Radiation (HRIR) observations in the 10μ window region of the spectrum. Since in this spectral region the transmissivity of the atmosphere above the highest clouds in a column is essentially one hundred percent, it follows from (9) that for the 10μ region

$$\xi^*(\nu, p_c) = \frac{\bar{I}(\nu) - I_{cl}(\nu)}{B(p_c) - I_{cl}(\nu)}$$

where $\bar{I}(\nu)$ is the average intensity leaving the atmosphere over the area of interest, $I_{cl}(\nu)$ is the average intensity leaving the clear columns within the area, and $B(p_c)$ is the average Planck radiance emitted by the clouds within the area. Since the areal resolution of HRIR measurements may be restricted to less than $5 km^2$, the lowest HRIR intensities measured within the area of interest may be interpreted as the Planck radiance $B(p_c)$, and the highest values as values of $I_{cl}(\nu)$, since in these extreme cases the field of view of the radiometer should tend to be completely filled by opaque clouds or clear of clouds, respectively. Hence, together with the entire area average value of the HRIR intensities, the effective emissivity of the clouds may be determined. An independent means of accurately determining the cloud pressure, p_c, from satellite observations of the absorption of reflected sunlight by molecular oxygen has been outlined by Wark and Mercer (1965).

3. METHOD OF INFERENCE

3.1 Physical Basis

Owing to the frequency dependence of the transmissivity function, the outgoing intensity in different frequency intervals is weighted toward different emitting levels in the atmosphere. At frequencies near absorbing band centers, only a small amount of absorbing gas is necessary to

hinder transmission; hence, most of the radiation lost to space at these frequencies originates from the upper levels of the atmosphere. On the other hand, at frequencies in the wings of absorbing bands, a significant amount of absorbing gas is necessary to hinder transmission; hence, most of the radiation lost to space originates from the lower levels of the atmosphere. It is this relation which enables vertical resolutions of atmospheric temperature and absorbing gas to be obtained from a set of outgoing radiation measurements in different frequency intervals.

Assuming that the surface and cloud characteristics (i.e., $\xi(\nu, p_o)$ and $\xi^*(\nu, p_c)$) are known, n independent observations of $I(\nu)$ provide a system of n simultaneous equations, each having the form of (9), which can be used to solve for n pieces of information about T(p) and q(p). However, there are experimental limitations on the total number of independent observations which can be obtained. Aside from a frequency resolution restriction, random instrumental errors restrict the ability to discriminate between the levels of the atmosphere contributing to the intensities of outgoing radiation, hence reducing any independence. There also exists a computational limitation on the number of independent observations which can be utilized to obtain a solution for temperature or absorbing gas due to the instability produced by random errors of measurement. Thus, any solution for temperature or absorbing gas must be obtained from relatively few radiation measurements.

Fortunately, as will be shown, the temperature distribution of the troposphere can usually be described adequately by as few as three pieces of information: (1) the surface temperature; (2) the average lapse rate near the ground (i.e., in the layer below the p_o - 50mb level); and (3) the average lapse rate of the troposphere above the (p_o - 50)mb level. Under the hydrostatic assumption, if the lapse rate $\gamma_1 = -\partial T/\partial z$ of a layer is constant, then the temperature at any pressure level in the layer may be given by:

$$T(p) = T(p_o)\left(\frac{p}{p_o}\right)^{\frac{\gamma_1 R}{g}} \qquad (10)$$

where R is the gas constant for dry air, g is the gravitational acceleration, and $T(p_o)$ is the surface temperature. The surface temperature for clear sky conditions may be estimated from a satellite measurement in a spectral region known as an "atmospheric window" where the attenuation by all the absorbing gases is at a minimum. Assuming that Eq. (10) describes the lower 50mb of the atmosphere, the lapse rate for this region may be given by:

$$\gamma_1 = \frac{g}{R}\left(\frac{\text{Log}[T(p_o - 50)/T(p_o)]}{\text{Log}[(p_o - 50)/p_o]}\right) \tag{11}$$

In a similar manner, the temperature distribution of the troposphere above the $(p_o - 50)$mb level may be given for a constant lapse rate γ_2 as:

$$T(p) = T(p_o - 50)\left(\frac{p}{p_o - 50}\right)^{\frac{\gamma_2 R}{g}} \tag{12}$$

Since CO_2 is evenly distributed in the atmosphere, having a constant depth of 0.245 cm/mb, the outgoing radiation in a region of a CO_2 band where water vapor absorption is at a minimum is primarily a function of the temperature distribution. Two observations in the low wave length side of the 15 micron CO_2 band and one observation in the 10 micron water vapor window region are best suited to be used to infer the lapse rates γ_1 and γ_2, and $T(p_o)$, respectively, and, hence, the temperature distribution of the lower atmosphere since the energy emitted at these frequencies is a maximum. However, the transmittances in these spectral regions are slightly dependent on the water vapor distribution of the troposphere. Hence, aside from its significant meteorological value in its own right, it is necessary to simultaneously obtain a reasonable estimate of the tropospheric water vapor distribution in order to obtain an accurate estimate of the temperature profile for the lower atmosphere.

For the purposes of this study, the water vapor distribution of the troposphere may be described by:

$$w(p) = w(p_o)\left(\frac{p}{p_o}\right)^{\lambda} \tag{13}$$

where $w(p)$ is the water vapor mixing ratio. It follows from (4) that the power λ which describes the moisture lapse is given uniquely for the entire atmospheric column by:

$$\lambda = \frac{w(p_o)p_o}{gu} - 1 \tag{14}$$

where u is the total precipitable water in the column. As is subsequently shown, infrared observations in the wings of the rotational and 6.3 micron bands of water vapor may be utilized to provide reasonable estimates of the coefficients $w(p_o)$ and λ.

Utilizing Eq. (9), a solution for the parameters $T(p_o)$, γ_1, γ_2, $w(p_o)$, and λ may be obtained simultaneously from a set of five radiation measurements if each measurement is independently weighted toward one of the parameters when the other four are specified. Figure 1 illustrates the vertical dependence for five theoretical satellite measurements in different frequency channels which satisfy the above criteria. The actual contribution to the outgoing intensity within the frequency interval $\nu_1 - \nu_2$ by any level p above the surface is given by:

$$\int_{\nu_1}^{\nu_2} B[\nu, T(p)] \frac{\partial \tau[\nu, u(p)]}{\partial p} \, d\nu \qquad (15)$$

while the surface contribution is given by:

$$\frac{1}{p_o} \int_{\nu_1}^{\nu_2} B[\nu, T(p_o)] \, \tau[\nu, u(p_o)] \, d\nu \qquad (16)$$

The relative contribution shown in Figure 1 at any level is defined by the ratio of the actual contribution at that level to the maximum contribution given by any level in the column. It should be noted here that all the radiation computations in this paper are based on the generalized absorption coefficients, illustrated in Figure 2, and procedure given by Elsasser (1960). The transmission function $\tau[\nu, u(p)]$ is specifically $\tau[\log l_\nu(T(p)) + \log u(p)]$. The computation performed to arrive at Figure 1 was made assuming: (1) the temperature structure of the U. S. Standard Atmosphere, (2) a typical mid-latitude moisture distribution, and (3) cloudless sky conditions and a surface emissivity of one. These temperature and moisture distributions are shown in Figure 3. Although changes in the temperature and moisture profiles may result in large changes in the actual contribution at any level, the relative contribution will not change significantly.

The curves shown in Figure 1 reveal which satellite measurements in the various channels are related most significantly to each parameter of the temperature and moisture model postulated above. The significance of any solution which might be obtained depends on certain necessary conditions. In the first place, it is vital that the three channels (i.e., 1, 3, and 5) which are most significantly related to γ_2, γ_1, and $T(p_o)$ respectively, are not greatly dependent on the water vapor distribution. It is apparent from the absorption coefficients illustrated in Figure 2 that this condition is fulfilled since in these spectral regions water vapor absorption is at a minimum. It is further necessary that the water vapor channels, 2 and 4, which are to be related to λ and $w(p_o)$, be weighted in the same atmospheric regions as the other channels since any water vapor solution obtained from

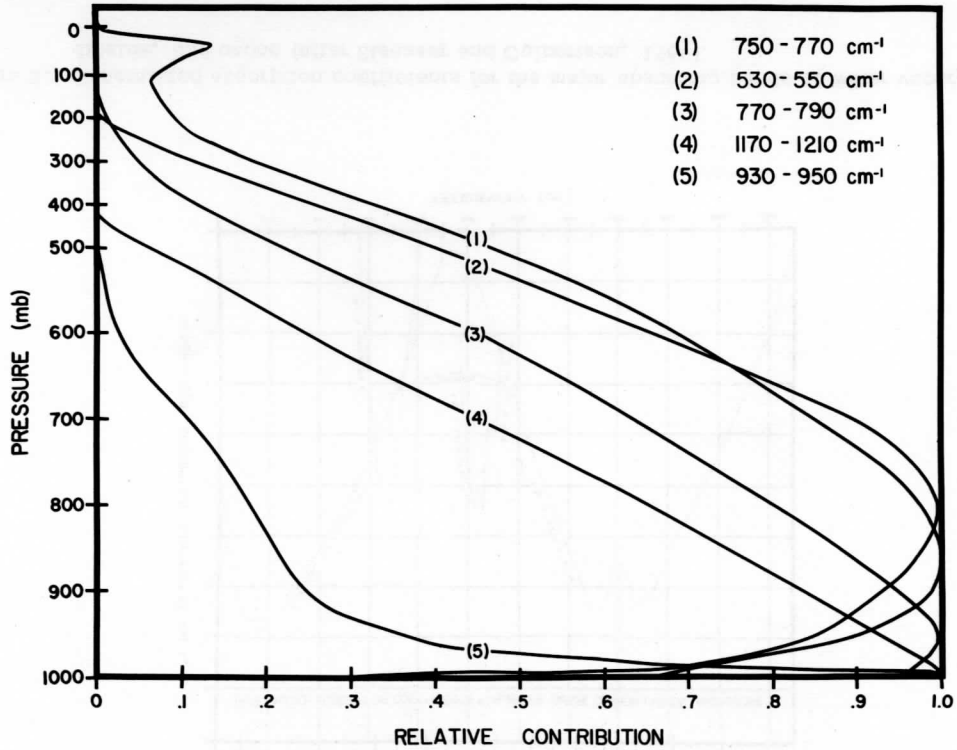

Figure 1. Relative contribution to the outgoing radiance in five theoretical satellite channels. These curves reveal which atmospheric layers the measured radiance is most heavily dependent upon.

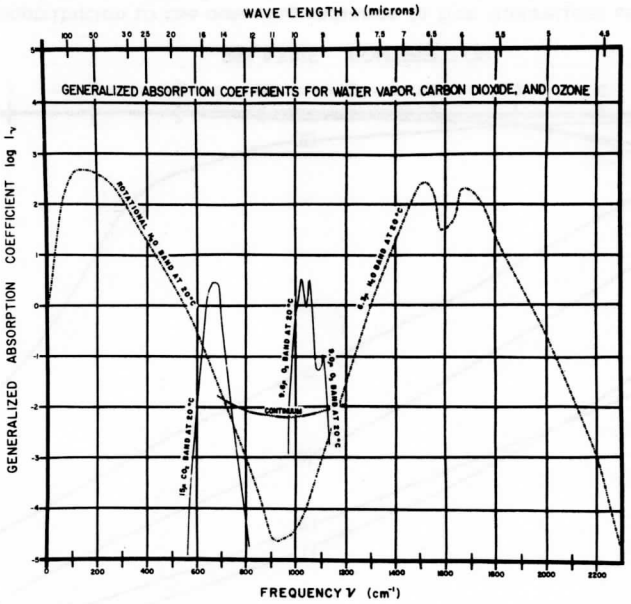

Figure 2. Generalized absorption coefficients for the major absorbing bands of water vapor, carbon dioxide, and ozone (after Elsasser and Culbertson, 1960).

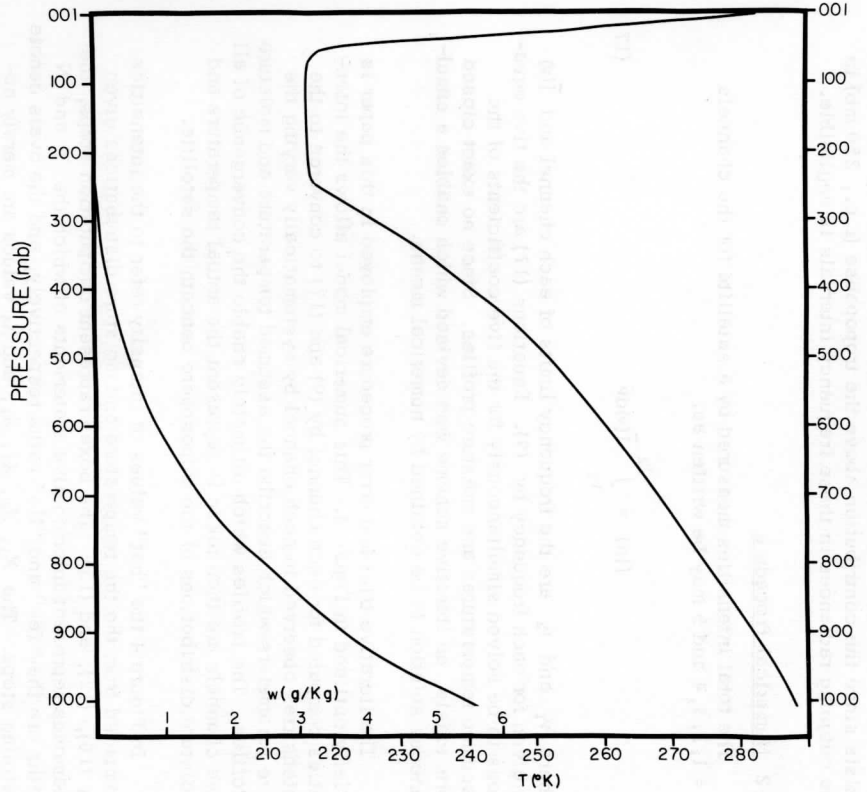

Figure 3. Hypothetical moisture and U. S. Standard Atmospheric temperature distribution.

these measurements will depend substantially on the exactness of the solution for temperature. It should also be mentioned that no serious overlap may exist among the three channels used to determine the temperature distribution or between the two used to determine the moisture distribution, since this would lead to a family of solutions. Finally it is desired that the solution for the temperature and moisture distribution of the troposphere be completely independent of a simultaneous solution for the upper atmosphere. As shown in Figure 1, this feature exists since the contribution above the tropopause (i.e., 250 mb) to the outgoing radiances in these frequency intervals is negligible.

3.2 Numerical Procedure

The total intensities measured by a satellite for the channels n = 1, 2, 3, 4 and 5 may be written as:

$$I(n) = \int_{\nu_1}^{\nu_2} \bar{I}(\nu)d\nu \qquad (17)$$

where ν_1 and ν_2 are the frequency limits of each channel and $\bar{I}(\nu)$ is given for each frequency by (9). Equations (17) are the five equations to be solved simultaneously for the five coefficients of the assumed temperatures and moisture profiles. Since no exact closed form exists, an iterative scheme was devised which enables a simultaneous solution to be obtained by numerical means.

The iterative trial and error procedure employed in this paper is briefly outlined in Figure 4. This numerical model allows the intensities computed for each channel by (9) and (17) to converge to the intensities observed in each channel by systematically varying the five parameters which describe the assumed temperature and moisture profiles. The profiles which ultimately enable the convergence of all five channels are then taken to represent the actual temperature and moisture distributions of the troposphere beneath the satellite.

In Figure 4 the "hat" values of intensity refer to the intensities computed from the the temperature and moisture distributions given by (10), (12), and (13). The boxes represent computation steps, the diamonds represent interrogative statements of which the Y and N paths are the "Yes" and "No" paths respectively, and the ovals denote defining steps. The X_1, X_2, X_3, X_4, and X_5 values are merely numerical variables which allow for the reduction of the step increments to the point necessary for convergence.

Since the temperature distribution yields some insight into the moisture distribution (e.g., mixing ratio inversions are frequently associated with strong temperature inversions) and indeed establishes

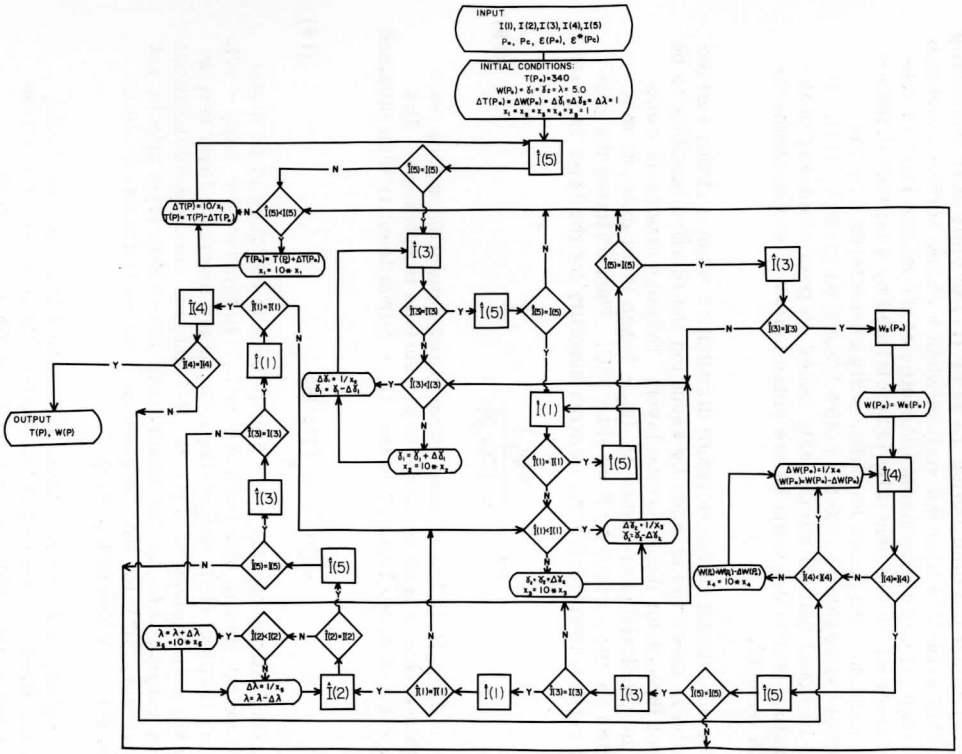

Figure 4. Flow diagram illustrating the numerical procedure utilized to obtain a simultaneous solution for the temperature and moisture distribution of the troposphere.

the maximum ratio the atmosphere may sustain (i.e., its saturation value), the predicted temperature profile is utilized with the observed radiance within the water vapor channels to estimate the water vapor profile. Specifically, aside from obtaining the computed radiances in the H_2O channels, the predicted temperature profile is incorporated to: (1) restrain the inferred mixing ratio from exceeding its saturation value; (2) adjust the distribution given by (13) to yield more physically reasonable estimates near the surface when a strong surface inversion exists; and (3) yield reasonable estimates of the mixing ratio in sub-cloud layers which are generally characterized by a uniform distribution of moisture and hence not adequately characterized by the analytical representation for the entire column as given by (13). It should be noted that all adjustments based on prior estimates of the temperature profile are made before obtaining any computed radiance in each channel.

The adjustment of the moisture distribution when a strong surface inversion is predicted is made by assuming the relative humidity to be constant throughout the inversion layer. This assumption is made when the predicted temperature of $(p_o - 50)$mb level exceeds that predicted for the surface by more than 5° C. Then utilizing the predicted surface temperature the relative humidity for the layer is given by:

$$Rh = \frac{w(p_o)}{w_s[T(p_o)]} \tag{18}$$

where $w_s[T(p_o)]$ is the surface value of the saturation mixing ratio as obtained from a prior estimate of the surface temperature. The mixing ratio of every level up to the $(p_o - 50)$mb level is then obtained from:

$$w(p) = w_s[T(p)]Rh \tag{19}$$

The mixing ratio above the $(p_o - 50)$mb level is assumed to be given by (13) except that in this instance $w(p_o)$ is replaced by $w(p_o - 50)$. Utilizing (18) and (19), the mixing ratio of the inversion layer may be set by the convergence of $\hat{I}(4)$ to $I(4)$ through successive iterations made by varying $w(p_o)$. The mixing ratio above this layer may be set by converging $\hat{I}(2)$ to $I(2)$ through successive iterations made by varying the λ value of Eq. (13).

A slightly different procedure is followed if clouds are noted within the field of view of the radiometer. In this case the mixing ratio at the cloud level is restrained to follow the relation:

$$w(p_c) = \varepsilon^* w_s[T(p_c)] + (1 - \varepsilon^*) w_{cl}(p_c) \tag{20}$$

where ξ^* is the effective emissivity and $w_{cl}(p_c)$ is that mixing ratio which would exist at p_c in the absence of clouds and is assumed to be given by Eq. (13) from the initial or prior estimate of λ. The mixing ratio distribution below the cloud level is assumed to follow (13) for the lambda value:

$$\lambda_1 = \frac{\log [w(p_c)/w(p_o)]}{\log [p_c/p_o]} \tag{21}$$

The mixing ratio below the clouds may then be set by the convergence of $\hat{I}(4)$ to $I(4)$ through iterations based on Eq. (13) for various $w(p_o)$ and subsequently various λ_1 values. The moisture distribution is specified between the p_c and $(p_c - 50)$mb levels by:

$$w(p) = w(p_c)\left(\frac{p}{p_c}\right)^{\lambda_2} \tag{22}$$

where

$$\lambda_2 = \frac{\log [w(p_c - 50)/w(p_c)]}{\log[(p_c - 50)/p_c]}$$

and above the $(p_c - 50)$mb level by (13) where λ is determined through successive iterations of $I(2)$. This procedure allows $\lambda_1 \rightarrow \lambda_2 \rightarrow \lambda$ as $\xi^* \rightarrow 0$.

4. SIMULATED TRIALS

A sufficient test of the inference model developed here requires the direct comparison of the temperature and moisture profiles inferred from actual satellite observations with the temperature and moisture profiles observed by radiosondes. Unfortunately there are no radiation observations pertaining to the channels shown in Figure 1 presently available for such a comparison. However, a simulated trial of the inference model may be made by using simulated satellite radiance measurements. The procedure involves the assumption that the true radiance in the various channels leaving the atmosphere can be computed from the actual temperature and moisture profiles. Then using this information as the satellite input data in the inference model, an attempt can be made to recover the temperature and moisture distribution of the troposphere. Figures 5 to 8 show the results of this procedure for a set of clear soundings representing typical but widely different synoptic situations. In these figures the dashed curves are the radiosonde observed soundings as tabulated by Wark, Yamamoto, and Lienesch (1962) whereas the solid curves are the soundings predicted by the model utilizing the simulated satellite observations. In all of these trials the initial

Figures 5 - 8 (pages 17 - 20, respectively). Solutions of the tropospheric structure of typical clear sky situations. The dashed lines represent the observed soundings and the solid lines the inferred soundings. The solid Z' line at the right hand side illustrates the differences between the heights of various pressure levels in meters as calculated from the radiosonde observed and satellite inferred temperature soundings (i.e., Z' = Z (radiosonde) - Z (satellite)).

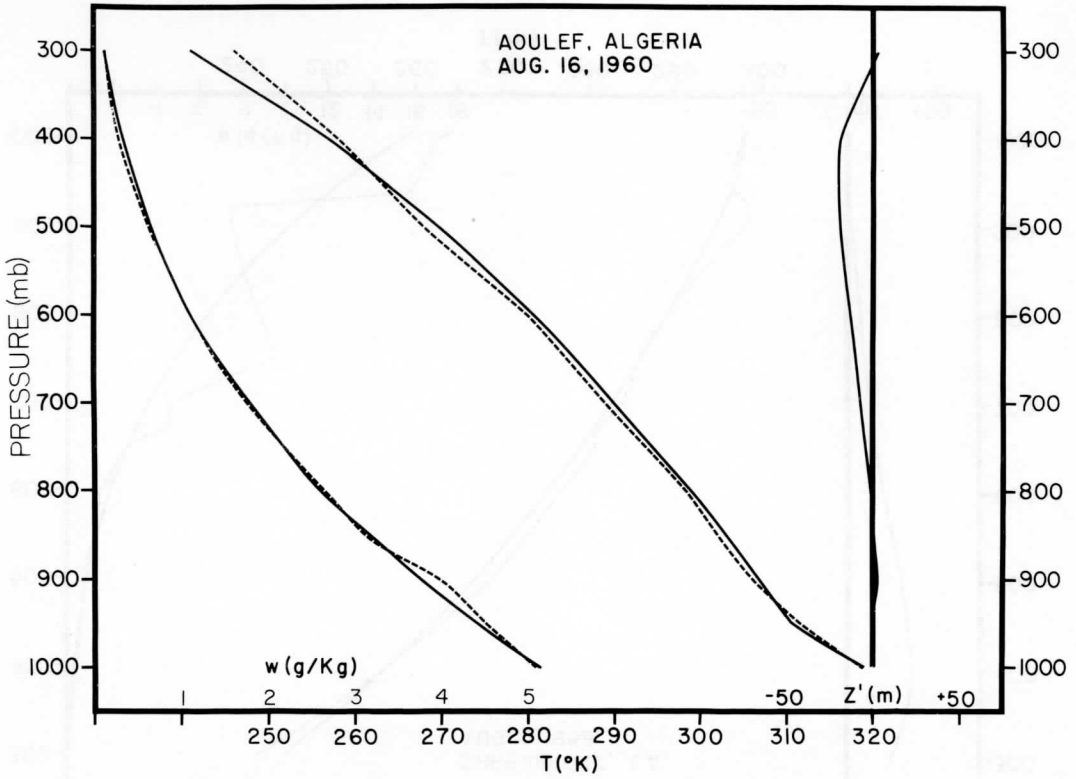
AOULEF, ALGERIA
AUG. 16, 1960
PRESSURE (mb)
300
400
500
600
700
800
900
1000
w (g/Kg)
1
2
3
4
5
-50
Z'(m)
+50
250
260
270
280
290
300
310
320
T(°K)

Figure 5

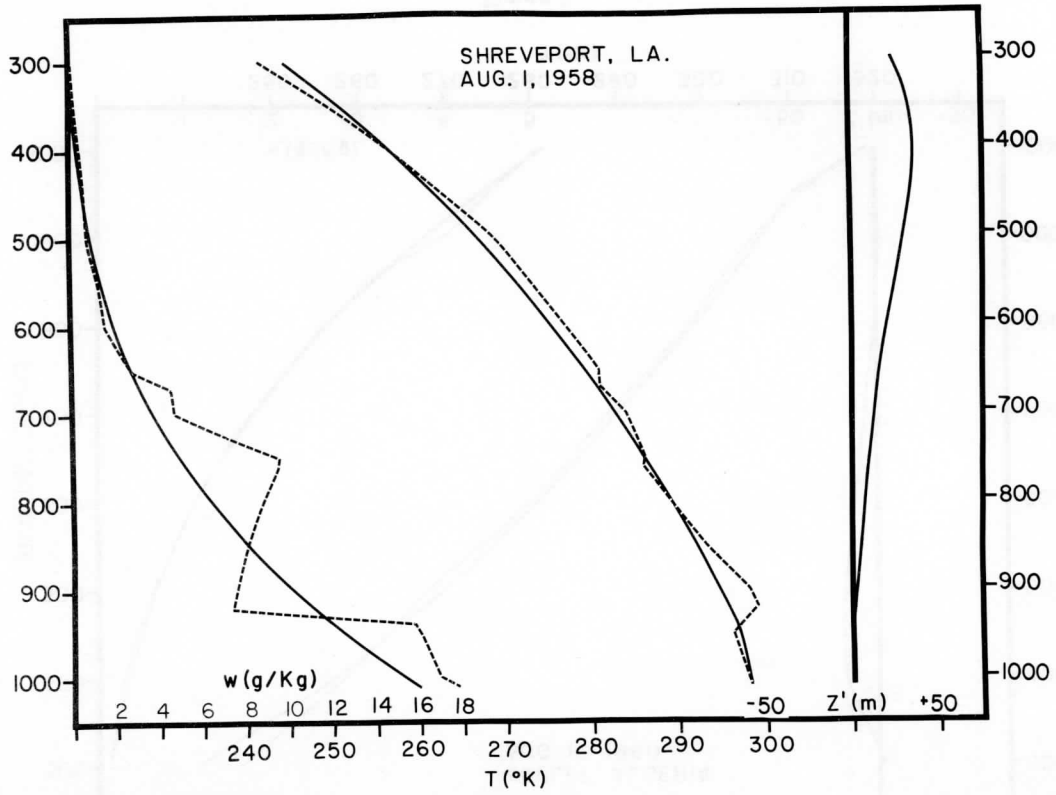
SHREVEPORT, LA.
AUG. 1, 1958
300
400
500
600
700
800
900
1000
w (g/Kg)
2 4 6 8 10 12 14 16 18
240 250 260 270 280 290 300
T (°K)
-50
Z' (m)
+50

Figure 6

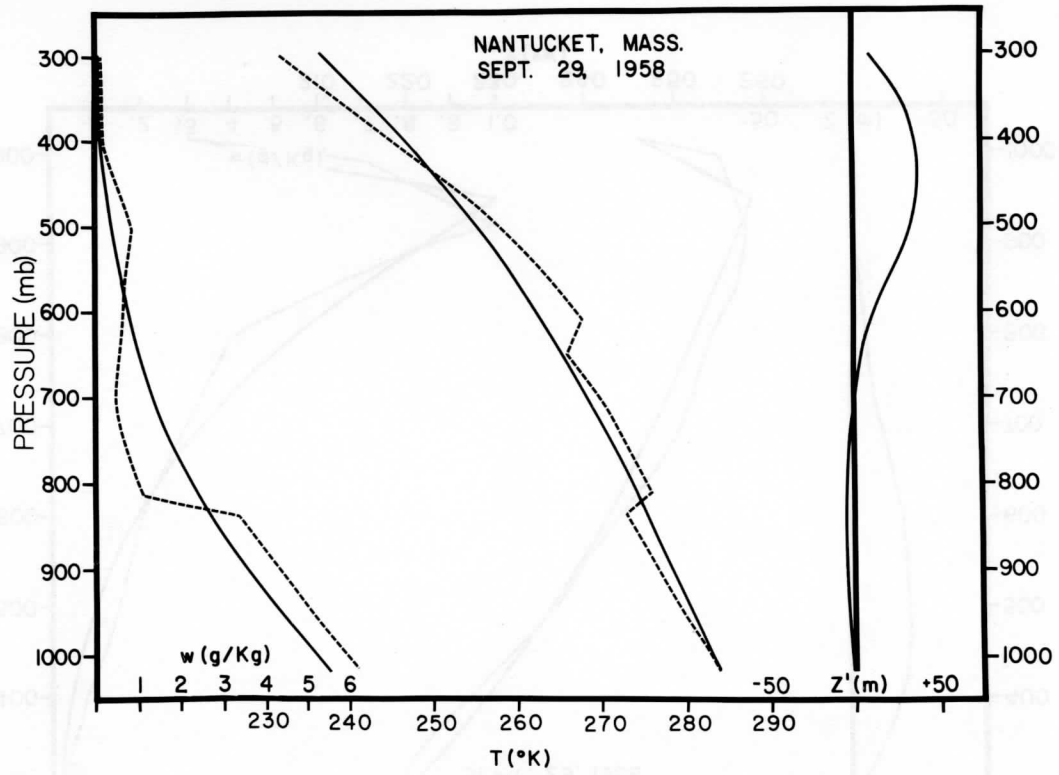
NANTUCKET, MASS.
SEPT. 29, 1958
PRESSURE (mb)
300
400
500
600
700
800
900
1000
w (g/Kg)
1 2 3 4 5 6
230 240 250 260 270 280 290
T (°K)
-50 Z'(m) +50

Figure 7

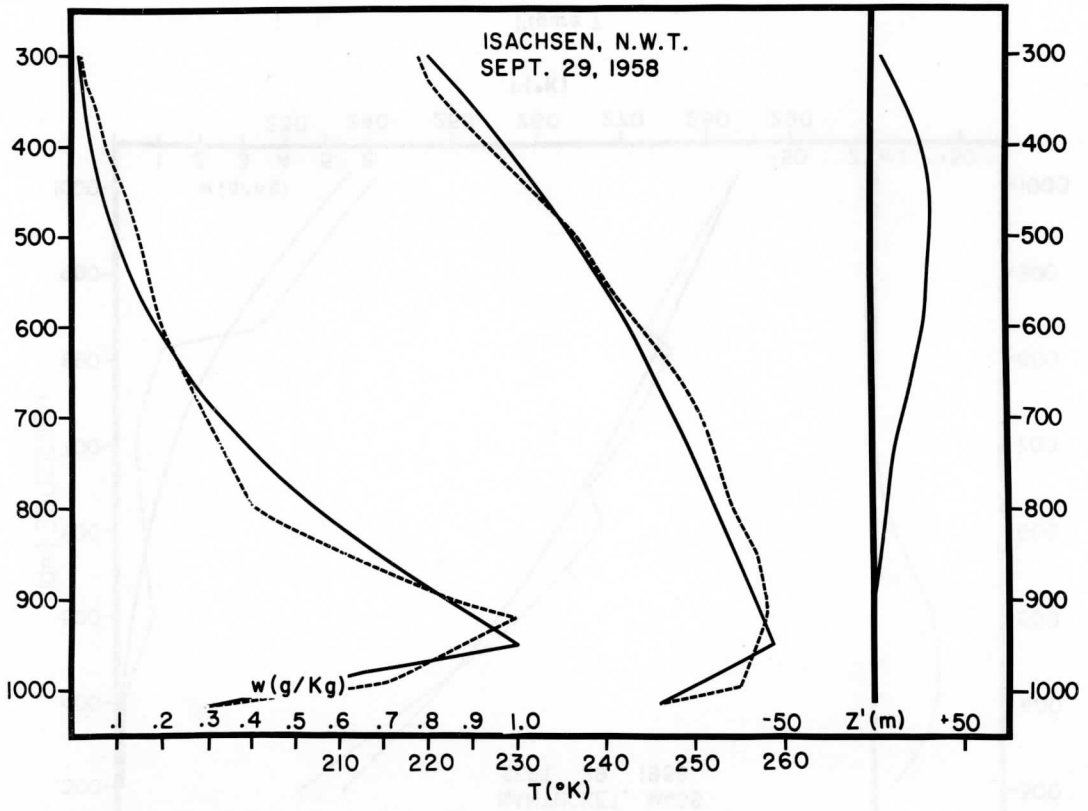
ISACHSEN, N.W.T.
SEPT. 29, 1958
300
400
500
600
700
800
900
1000
w(g/Kg)
.1 .2 .3 .4 .5 .6 .7 .8 .9 1.0
210 220 230 240 250 260
T(°K)
-50 Z'(m) +50

Figure 8

conditions were taken as those shown in Figure 4. The convergence criteria for these trials was chosen so that the computed radiances were only required to be within one-half of one percent of the satellite observed values. The solutions were conducted on a 3600 CDC digital computer. The time required to obtain the temperature and moisture solutions is about five seconds per sounding on this machine.

The observed sounding shown in Figure 5 is representative of the type the model is capable of predicting almost perfectly since its physical characteristics very nearly satisfy the analytical forms assumed. The ability of the model to recognize the slightly stronger lapse of temperature near the surface is noteworthy. The sounding shown in Figure 6 is characterized by almost the same mean tropospheric temperature as that pertaining to the sounding in Figure 5. The significant differences in moisture content and temperature lapse rates which exist, however, were adequately predicted. The inability to predict temperature and moisture discontinuities aloft is illustrated by both Figures 6 and 7 whereas the ability to account for discontinuities near the surface is demonstrated in Figure 8. In all the above cases the average vertical profiles, especially the temperature profiles are predicted extremely well. This feature is also evident from the relatively small differences between the radiosonde observed and satellite predicted values of the heights, Z', of the various pressure levels.

Figures 9 to 12 reveal the results of the predictions of soundings associated with an overcast. The effective emissivities of the clouds were estimated from the degree of saturation which existed at the cloud levels. It must be borne in mind that the amount of information about the structure of the sub-cloud layer which is inherent in the satellite observations decreases as the effective emissivity approaches unity. However, even when no information may be obtained ($\xi^* = 1$), as in the case illustrated in Figure 12, a prediction for the sub-cloud layer is still obtained which is consistent with the modelling assumptions and the solution obtained for the region above the cloud. The ability of the model to utilize the information obtained below regions of relatively sparse cloudiness is illustrated in Figure 9. Owing to the relatively low effective emissivity, the inversion near the surface was predicted. It is also shown that even in the cloudy cases reasonable approximations of the pressure-height relationship can be obtained.

Table 1 illustrates the relation between the observed and predicted surface temperature, T_o, mean tropospheric lapse rate, $\bar{\gamma}$, mean temperature of the surface to 300-mb layer, $\bar{T}$, surface mixing ratio, w_o, and total precipitable water, U. The soundings 1 - 8 correspond with those shown in Figures 5 - 12, respectively. These results reemphasize the ability of the model to arrive at the general temperature and moisture characteristics of the troposphere from the proper satellite

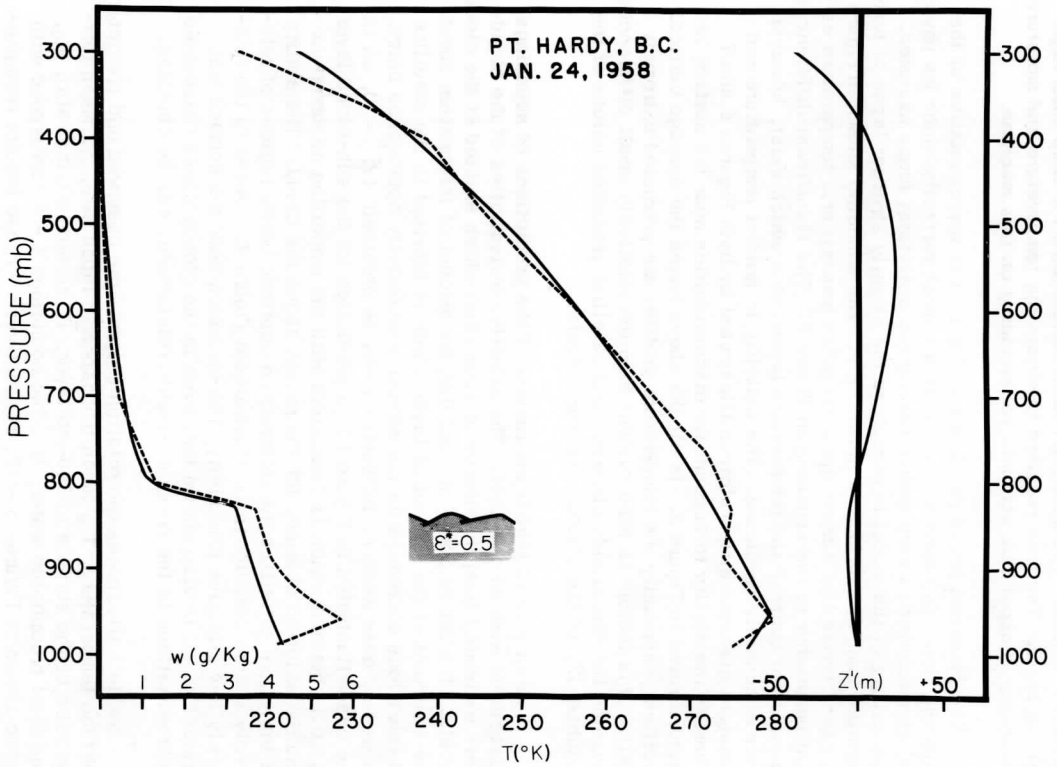

Figure 9. Solutions of the tropospheric structure of typical cloudy sky situations.

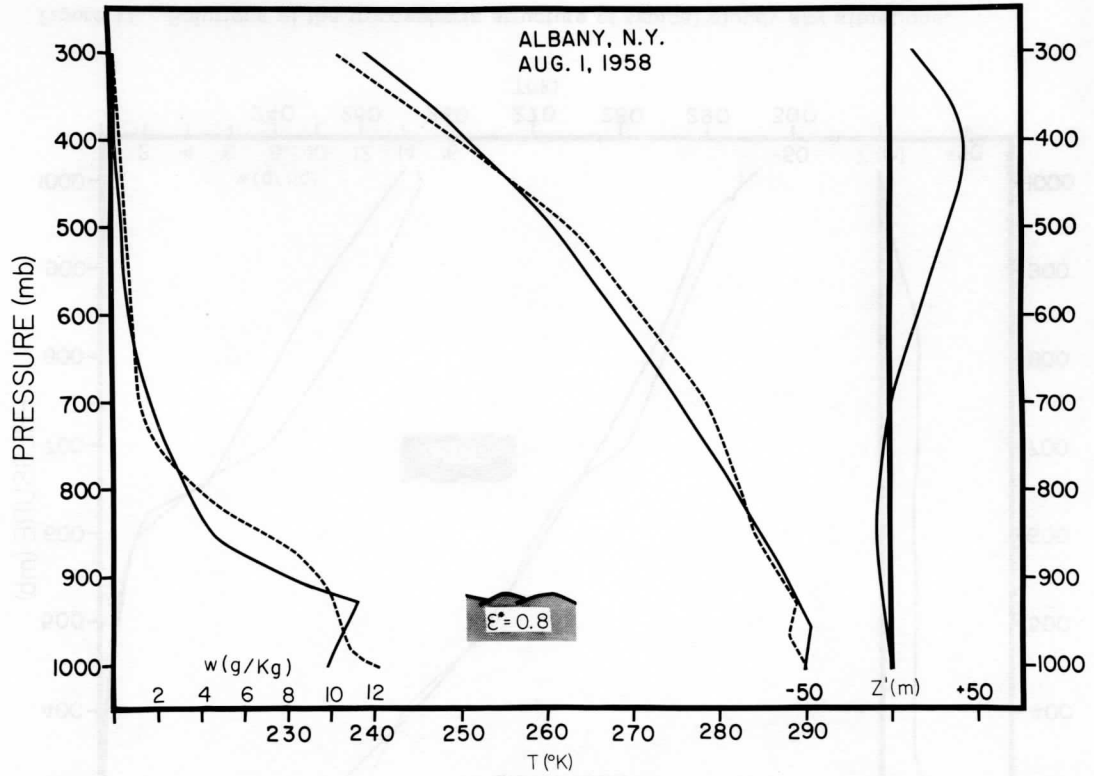

Figure 10. Solutions of the tropospheric structure of typical cloudy sky situations.

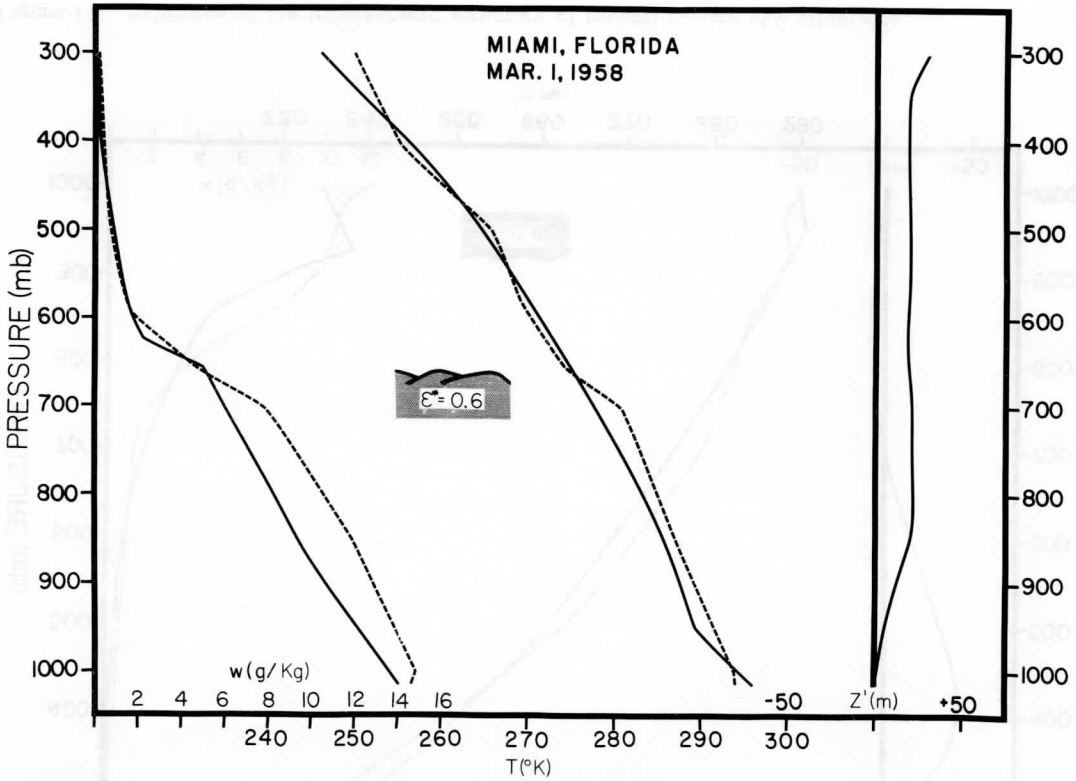

Figure 11. Solutions of the tropospheric structure of typical cloudy sky situations.

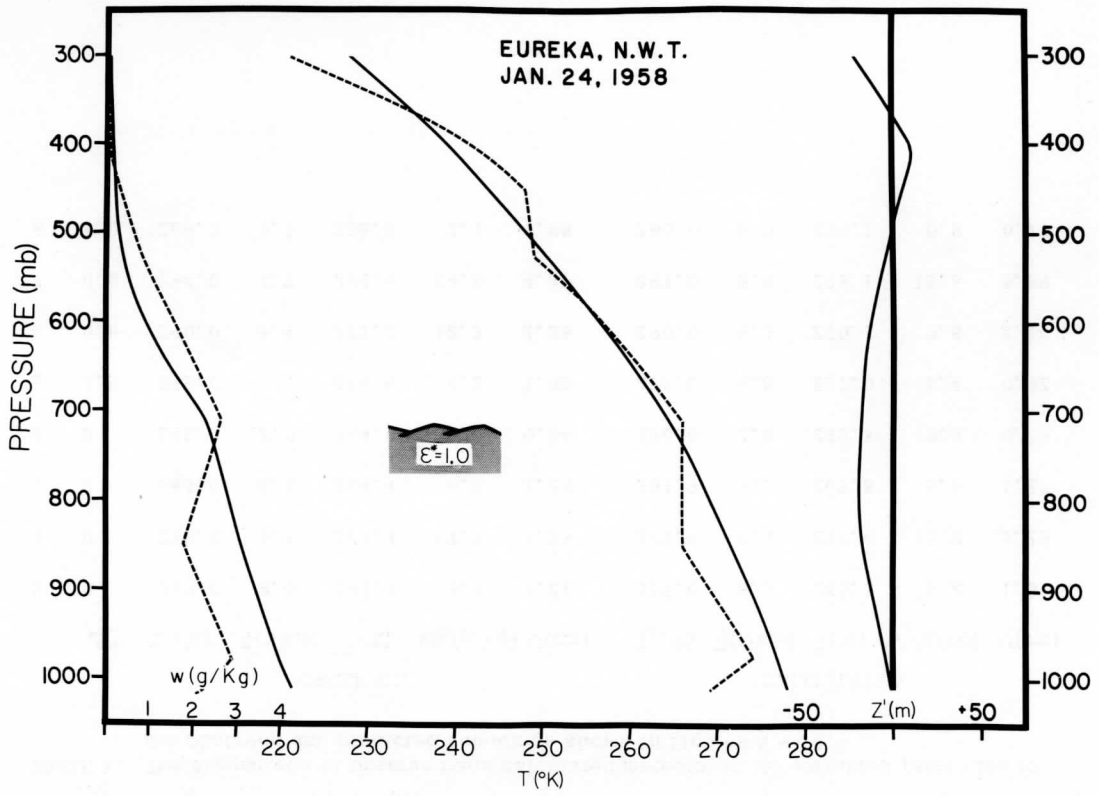

Figure 12. Solutions of the tropospheric structure of typical cloudy sky situations.

TABLE 1. The comparison of observed and calculated meteorological variables pertaining to the observed and predicted soundings shown in Figures 5 - 12.

		OBSERVED					CALCULATED				
	ε^*	T_o(°K)	$\bar{\gamma}$(°/km)	$\bar{T}$(°K)	W_o(g/kg)	U(cm)	T_o(°K)	$\bar{\gamma}$(°/km)	$\bar{T}$(°K)	W_o(g/kg)	U(cm)
1	0	319.0	8.0	283.0	5.1	1.27	319.0	8.3	283.3	5.2	1.31
2	0	298.0	5.5	277.9	17.8	3.73	279.9	5.4	277.0	15.9	3.25
3	0	284.0	5.4	264.4	6.2	1.20	283.9	5.2	263.8	5.5	1.21
4	0	246.0	2.0	244.0	0.3	0.24	246.0	2.0	243.3	0.3	0.25
5	0.5	275.0	5.8	256.6	4.2	1.05	278.0	5.8	257.0	4.4	0.92
6	0.8	290.0	5.4	271.1	12.2	2.25	290.0	5.3	270.1	9.8	2.10
7	0.6	294.0	4.7	274.5	14.6	4.47	293.0	5.0	273.1	15.6	3.89
8	1.0	269.0	4.5	256.2	2.1	1.08	280.0	6.0	259.1	0.9	0.77

radiation measurements, even for the convergence criteria of one-half of one percent. This indicates that the model behaves in an extremely stable fashion.

In order to determine the ability of the inference model developed here to utilize radiation observations to deduce synoptic scale meteorological features, outgoing radiance measurements were calculated from the temperature, dewpoint, and cloud data displayed on the Northern Hemisphere surface and constant pressure level charts supplied by the Numerical Analysis Center of the U. S. Weather Bureau. Specifically, the charts pertaining to 1200 G. C. T. December 24, 1960, were utilized. From these charts temperatures, dewpoints, cloud amounts, and the relative cloud heights (i. e., low, middle, or high) were interpolated to grid points spaced 5° in latitude and longitude between 30 - 60° North and 50 - 135° West. From the interpolated data, soundings of temperature and mixing ratio were constructed at each of the ninety-eight grid points. The effective cloud pressure levels for each grid point were then estimated from the interpolated soundings. From the observed grid point soundings and the interpolated cloud information the outgoing radiance in each channel was calculated. Then utilizing these simulated satellite observed radiances and the observed cloud parameters as input data in the inference model, the satellite predicted temperature and moisture profiles were obtained. Since all clouds were assumed to be black, the effective emissivity was equal to the observed fractional cloud cover interpolated for each grid point.

Figure 13 shows the observed sea level isobars analyzed at every four millibars and the isolines of equivalent blackbody temperature (°K) pertaining to the radiances calculated from the grid point soundings. The numbers ranging between zero and one on the sea level chart are the estimated effective emissivity of the clouds in the grid area. The equivalent temperatures for Channel (5) are nearly equal to the surface temperature in clear areas since the attenuation by water vapor of the surface radiance is extremely small in this spectral region. In such areas differences between the Channel (4) and (5) equivalent temperatures might be interpreted in terms of low level moisture, however, since the additional attenuation by water vapor in the Channel (4) radiance is only about 3°K, these differences are not revealed adequately on the charts shown in Figure 13 owing to the resolution of the analysis. The Channel (1) and Channel (3) equivalent temperatures may be interpreted in cloudless areas in terms of the mean temperatures of the middle and lower troposphere, respectively. The almost equal equivalent temperatures obtained for Channels (1), (3), and (5) at the high latitudes reflect the near isothermal conditions which generally exist in winter at these latitudes.

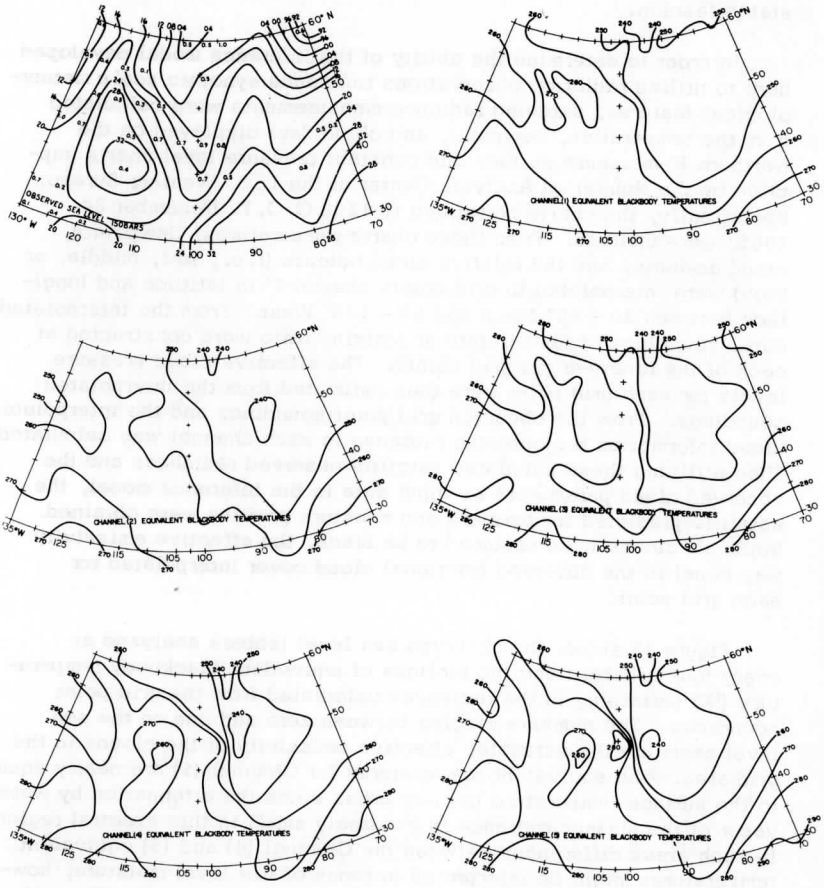

Figure 13. Synoptic maps of sea level pressure in millibars (thousands and hundreds digits omitted, 00 = 1000 mb, 96 = 996 mb, ...) and computed equivalent blackbody temperatures (°K) for 1200 G. C. T. December 24, 1960. The numbers ranging between zero and one on the sea level chart represent the mean fractional cloud cover observed in the grid area.

Figure 14 shows the observed and predicted height fields for the 850, 500, and 300 mb levels as calculated from the observed and predicted temperature soundings for each grid point. Since the observed surface pressure was utilized in the calculation of the predicted height fields, the information supplied by the inference model consisted of the thickness field. Thus errors in the predicted height patterns are due solely to errors in temperature. The 850 and 500 mb contours are drawn for 60 meter intervals while the 300 mb contours are drawn for 120 meter intervals. As can be seen from the results shown in Figure 14, the predicted and observed patterns are nearly identical, thus indicating that the errors inherent in the satellite predicted heights are within the resolution of ordinary synoptic analysis. The observed increase in the contour gradients as well as the change in position of the pressure centers with height is adequately revealed in the predicted patterns.

Figure 15 shows the observed and predicted specific humidity (g/kg) patterns at the surface and 850 mb levels and the isolines of tropospheric precipitable water (cm). As can be seen, the major features of the specific humidity patterns are inferred quite well from the radiation observations, especially in the clear areas. The lack of agreement in the cloudy regions is probably due to the assumption that the clouds are completely black since this assumption tends to lead to an overestimate of the mixing ratio at the cloud level as obtained by Eq. (20). The estimates of the total precipitable water inferred from the radiance observations agree quite well with the observed patterns, even in the cloudy areas.

Finally, mention should be made of the possible usefulness of the satellite predicted synoptic field in numerical forecasting. In a recent study summarized by Charney (1965), a relation is given between the rms temperature errors associated with the observed flow at the 800 and 400 mb levels and the number of days the flow at each level can be deterministically predictable. The rms temperature errors for the 800 mb and 400 mb levels computed from the observed and satellite predicted soundings pertaining to the synoptic illustration referred to above were about 1.7°C and 2.7°C, respectively. According to Charney the flow for each level whose temperatures are determined within these rms errors should remain deterministically predictable for about seven days. Hence, although the rms errors in the satellite predicted temperatures are significantly larger than the errors associated with radiosonde observations, the latter being less than 1°C, these errors are tolerable for short range numerical forecasts.

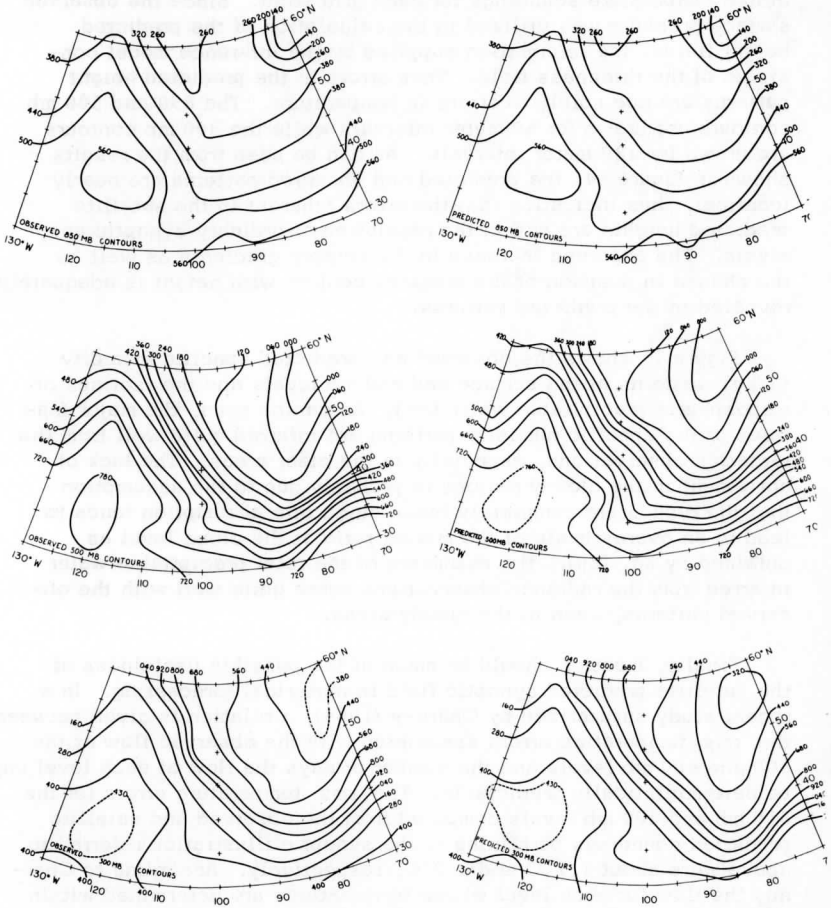

Figure 14. Observed and predicted height fields in meters (thousands digits omitted).

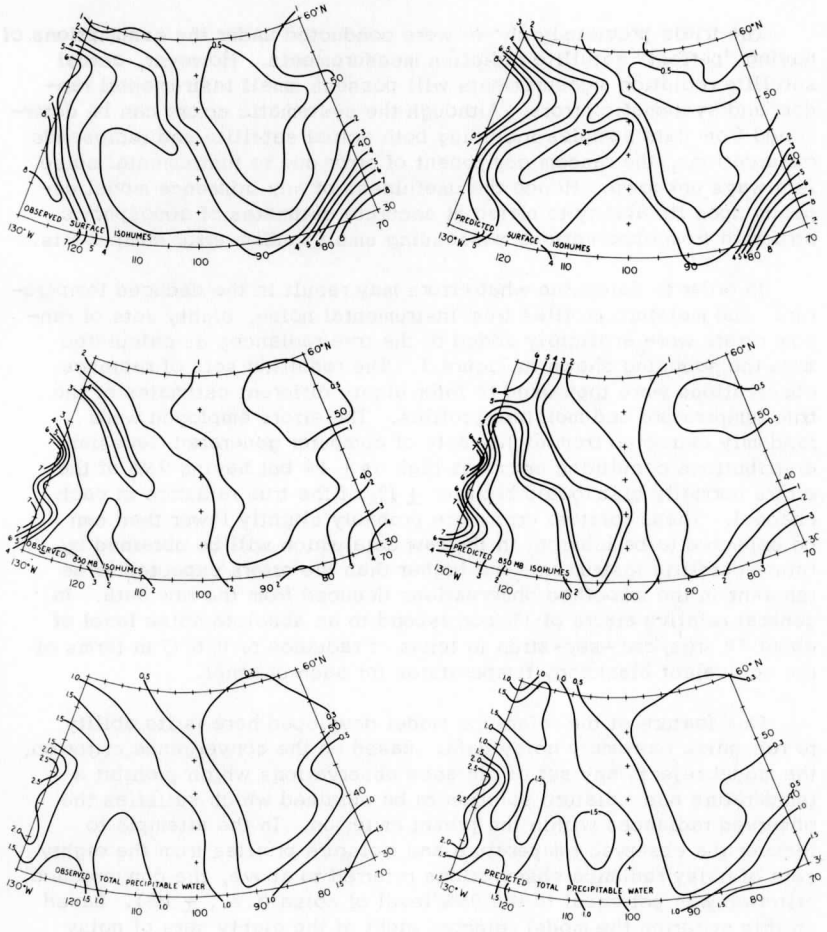

Figure 15. Observed and predicted moisture fields. The isohumes represent isolines of specific humidity in g/kg. The isolines of precipitable water are in centimeters.

5. INFLUENCE OF RANDOM AND SYSTEMATIC ERRORS

The trials previously shown were conducted under the assumptions of having "perfect" satellite radiation measurements. However, actual satellite radiation measurements will possess small instrumental random and systematic errors. Although the systematic errors can be determined from data samples including both actual satellite and radiosonde observations, the random component of error due to instrumental noise is always unknown. Hence the usefulness of any inference model depends upon its ability to arrive at accurate estimates of atmospheric structure from observations possessing small random error components.

In order to determine what errors may result in the deduced temperature and moisture profiles from instrumental noise, eighty sets of random errors were artifically added to the true radiances as calculated from the sounding shown in Figure 3. The resulting sets of radiance observations were then used to infer eighty different estimates of the true temperature and moisture profiles. The errors employed were randomly extracted from eighty sets of computer generated Gaussian distributions containing errors as high as $\pm$ 4% but having 95% of the errors normally distributed between $\pm$ 1% of the true radiance in each channel. These relative errors are probably slightly lower than can be expected to be inherent in the raw data which will be obtained by future satellite instruments but higher than the errors expected to be inherent in the smoothed observations deduced from the raw data. In general relative errors of 1% correspond to an absolute noise level of about 20 ergs/cm^2-sec-strdn in terms of radiance or 0.6°C in terms of the equivalent blackbody temperatures for each channel.

One feature of the inference model developed here is its ability to recognize extremely noisy data. Based on the convergence criterion, the model rejects any set of radiance observations which prohibit a temperature and moisture solution to be obtained which satisfies the observed radiances within the preset criterion. In the attempts to recover the observed temperature and moisture profiles from the eighty sets of noisy radiance observations referred to above, the convergence criterion was set equal to the 95% level of noise (i.e., $\pm$ 1%). Based on this criterion the model rejected eight of the eighty sets of noisy radiance observations.

Figure 16 shows the envelopes of the temperature and height errors at the 66% and 95% levels pertaining to the solutions obtained from the seventy-two admissable sets of radiance observations. The 66% and 95% levels are illustrated since they correspond to the 1σ (i.e., standard deviation) and 2σ levels of a normal distribution of errors. As can be seen from Figure 16, the standard deviation of the

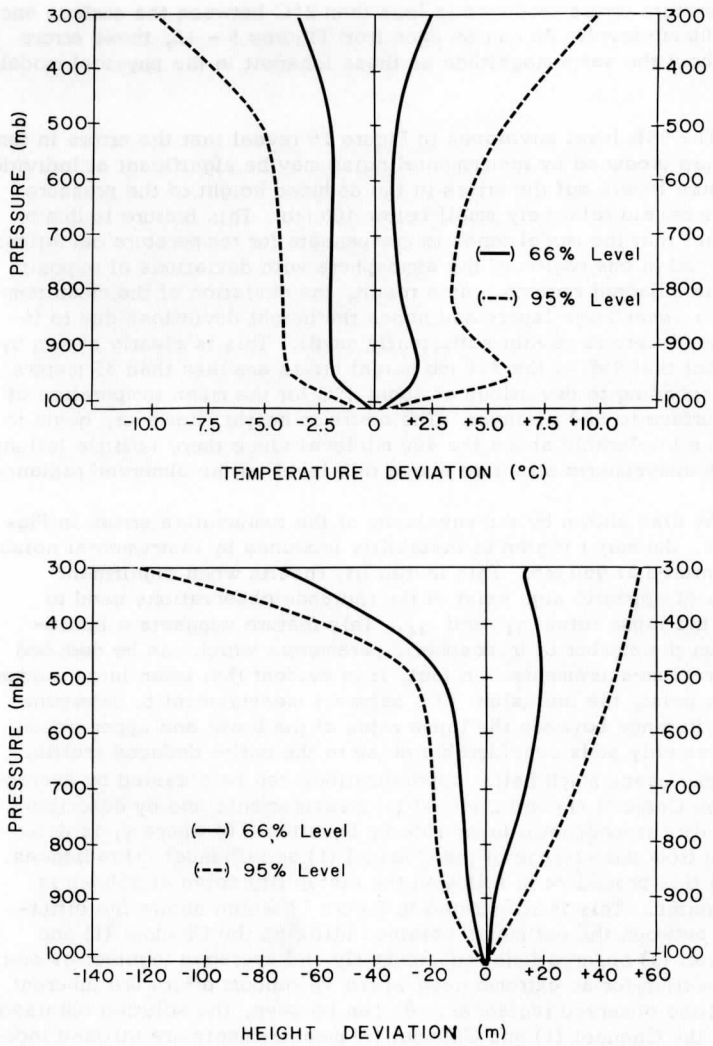

Figure 16. Envelopes of the temperature and height errors resulting from random errors induced into the true radiances calculated from the soundings shown in Figure 3. The dashed lines bound 95% of the resulting errors, whereas the solid lines bound 66% of the resulting errors.

temperature errors produced is less than 2°C between the surface and the 500 mb level. As can be seen from Figures 5 - 12, these errors are about the same magnitude as those inherent in the physical modelling.

The 95% level envelopes in Figure 16 reveal that the errors in temperature produced by instrumental noise may be significant at individual pressure levels but the errors in the deduced height of the pressure levels remain relatively small below 400 mb. This feature is due to the fact that the model tends to compensate for temperature deviations produced in one region of the atmosphere with deviations of opposite sign in adjacent regions. As a result, the deviation of the mean temperature over large layers and hence the height deviations due to instrumental errors remain sufficiently small. This is clearly shown by the fact that 95% of the 500 mb height errors are less than 35 meters corresponding to deviations of about 2°C for the mean temperature of the surface to 500 mb layer. The errors in height, however, begin to become intolerable above the 400 mb level since there is little influence of the atmospheric structure above this level on the observed radiances.

As also shown by the envelopes of the temperature errors in Figure 16, the major region of instability produced by instrumental noise is centered at 950 mb. This instability results when significant errors of opposite sign exist in the radiance observations used to infer the lapse rates γ_1 and γ_2. This feature suggests a limitation on the number of tropospheric parameters which can be deduced from real measurements. In fact, it is evident that when large random errors exist, the inclusion of a separate measurement to determine the difference between the lapse rates of the lower and upper tropospheres only adds considerable noise to the entire deduced profile. In these cases much better approximations can be obtained by averaging the Channel (1) and Channel (3) measurements and by describing the entire tropospheric lapse rate by Equation (10) where γ_1 is determined from the average of the Channel (1) and Channel (3) radiances. When this procedure is followed the instability noted at 950 mb is eliminated. This is illustrated in Figure 17 which shows the difference between the estimates obtained utilizing the Channel (1) and Channel (3) observations independently and averaged together as one observation for an extreme case where 3% random errors are inherent in all the observed radiances. As can be seen, the solution obtained when the Channel (1) and Channel (3) measurements are utilized independently is totally unrealistic on physical grounds, whereas significant information is still obtained by the model when the average value of the two radiances is employed. Due to the absurdity of the solution obtained in such extreme cases, it seems that the model may be able to distinguish between such cases when the two measurements should not be utilized independently.

Table 2 reveals the effect of instrumental noise of the order of 0.5°C, in terms of equivalent blackbody temperature, on estimates of other significant meteorological quantities. The standard deviations shown indicate that comparatively larger errors are produced in the moisture profile than in the temperature profile. This is expected since errors in the temperature profile as well as the errors in the measured radiance in the water vapor channels affect the approximation of the moisture distribution. However, it seems that if the rms value of random errors can be kept below 0.5°C, estimates of the total precipitable water, $U(p_o)$, might be obtained to within 20% of the actual value. This resolution is sufficient to distinguish between the moisture characteristics of the major types of air masses.

Finally, Figure 18 illustrates the effects of large systematic errors on profile estimates of temperature and moisture. The predicted profiles correspond to the two cases where all five radiances are biased too high or too low depending upon which sounding is assumed to be the observed, by three percent (i.e., approximately 60 ergs/cm²-sec-strdn or 2.5°C). In this case, the resulting error in the deduced height is about 13 m/km corresponding to a mean error of about 3°C through the layer. It is noted that similar systematic errors in the deduced profiles might result from undetected aerosol or thin cloud layers and errors in estimates of the actual cloud height and amounts which would have the effect of biasing the observed values higher or lower than those predicted from radiative transfer theory. Fortunately these errors should have little effect on the stability of the solutions obtained.

TABLE 2. Standard deviations of meteorological quantities predicted from radiance observation possessing random instrumental errors.

QUANTITY	OBSERVED VALUE	STANDARD DEVIATION
$T(p_o)$	288°K	0.8°C
$W(p_o)$	5.6 g/kg	1.3 g/kg
$\bar{T}$	263°K	1.2°C
$U(p_o)$	1.29 cm	0.25 cm
$\bar{\gamma}$	6.5°C/km	0.5°C/km
λ	3.5	0.5

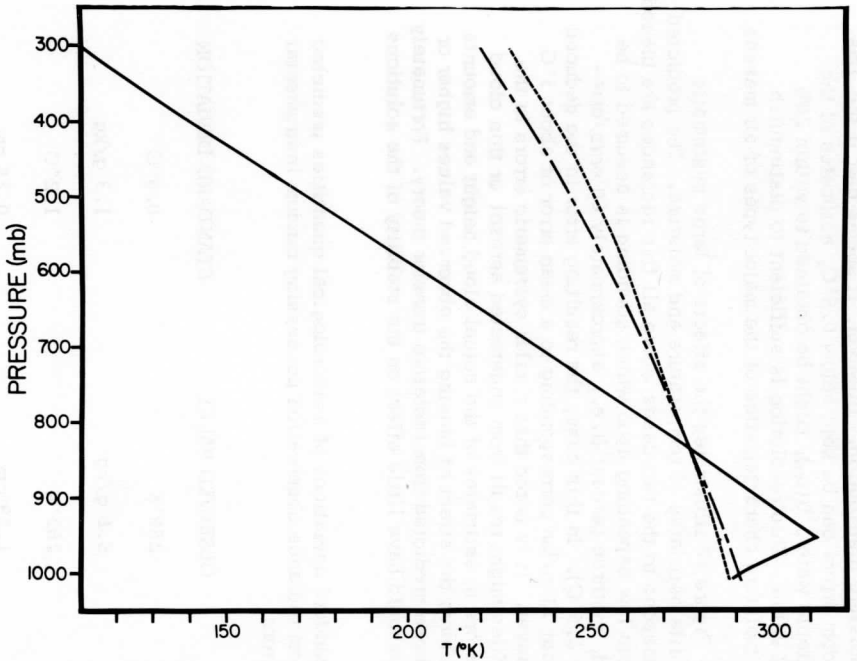

Figure 17. The unstable solution for temperature which is obtained when random errors of three percent, and of opposite sign in the Channel (1) and Channel (3) measurements, are inherent in all five observations. The dashed-dot line shows the solution obtained with the same distribution of random errors when the average value of the Channel (1) and (3) radiances are utilized in the inference model. The dashed line is the "observed" sounding.

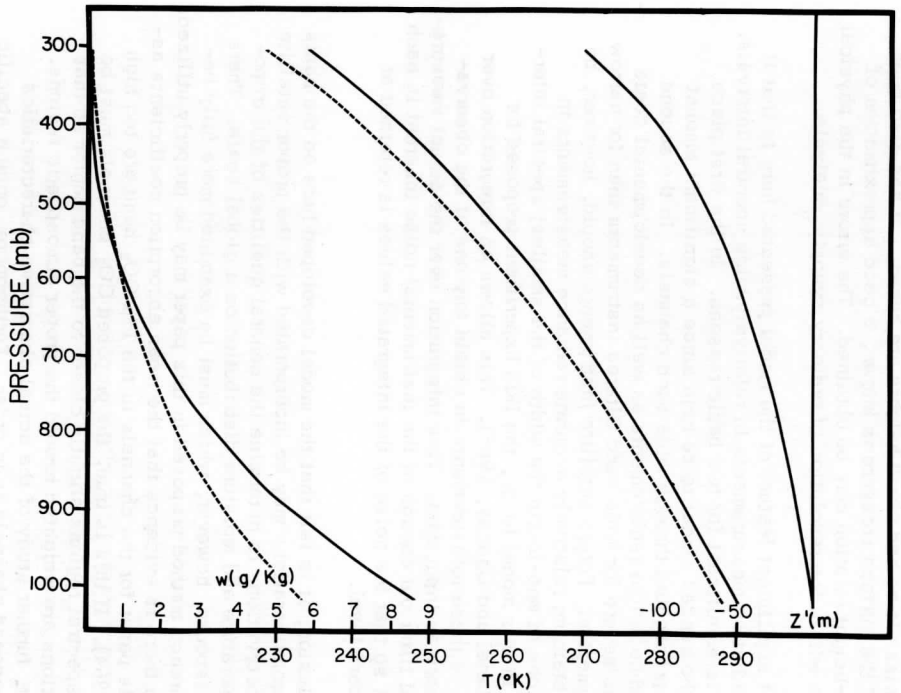

Figure 18. Solutions for temperature and moisture obtained if bias errors of three percent are inherent in all five radiance observations. The solid lines may be regarded as the predicted or observed soundings depending on whether the errors are biased too high or too low, respectively. In the calculations, however, the dashed lines were assumed to represent the observed conditions.

6. CONCLUSION

The model developed in this paper yields an indirect method of inferring tropospheric structure from satellite measurements. The technique is general enough to utilize many types of satellite measurements and may be applied regardless of cloud conditions, assuming the effective cloud emissivities and cloud heights are known. It has also been shown that if the surface pressure is known, a good approximation of the pressure-height relation may be obtained. The errors in the physical modelling are within the resolution of ordinary synoptic analysis.

The most significant feature of the model presented here is that it can utilize radiation measurements in relatively wide spectral intervals. This feature is significant for two basic reasons. In the first place this allows the sensed signal to be high since a significant amount of energy is propagated through wide band channels. In the second place the technological requirements as well as developmental costs are much less severe for wide band filtered instruments than for narrow band spectrometers. Future satellite instruments should, however, be capable of obtaining relatively accurate radiance measurements in spectral regions of one-fourth the width of the smallest spectral interval required in this model (e.g., the IRIS Experiment proposed for Nimbus B, Hanel and Chaney, 1965). This allows an integration over at least four of these measurements to obtain any one of the observations necessary as input data. This integration over the actual measurements should filter out enough of the instrumental noise inherent in each measurement so that the noise of the integrated values is retained at an insignificant level.

In conclusion, it is felt that the model developed here on the basis of physical considerations may be incorporated with the proper satellite and cloud observations to determine the general qualities of the tropospheric temperature and moisture distribution on a global scale. There are several aspects, however, which must be examined more fully before the inference method proposed in this paper may be properly utilized. For instance there is evidence that the mean absorption coefficients assumed in this paper for the channels in the 15μ CO_2 band are too high (Drayson, 1964). If this is true, the proposed CO_2 channels must be situated in spectral regions slightly closer to the band center so that the observations are weighted toward the proper atmospheric regions. In any event, further study of the actual absorptive characteristics of all the proposed channels is in order. Furthermore, once a specific satellite sensor employing the necessary radiation observations is operational, a careful study must be made to calibrate the model with respect to various cloud types and aerosol layers. This may be done from samples of corresponding satellite and radiosonde observations assuming the two effects (cloud and aerosol) may be separated.

ACKNOWLEDGMENTS

This investigation was supported by the National Weather Satellite Center of the National Environmental Services Administration. My thanks go to Professors V. E. Suomi and D. R. Johnson of the University of Wisconsin and Dr. D. Q. Wark and Mr. H. E. Fleming of the National Environmental Satellite Center for their helpful suggestions and criticisms throughout this research.

Finally, I wish to express my sincere gratitude to Professor Lyle Horn for his guidance throughout my graduate education.

REFERENCES

Butler, H. I., and H. S. Moore. "The Meteorological Instrumentation of Satellites," Goddard Space Flight Center, Greenbelt, Md., Sept. 1965. (Available from above address)

Chandrasekhar, S. Radiative Transfer. London: Oxford University Press, 1950.

Charney, J. G. "The Feasibility of a Global Observation and Analysis Experiment," A Report of the Panel on International Meteorological Cooperation to the Committee on Atmospheric Sciences, National Academy of Sciences, National Research Council, October, 1965.

Drayson, S. R. "Atmospheric Slant Path Transmissionin the 15μ CO_2 Band," Technical Report College of Engineering, High Altitude Engineering Laboratory University of Michigan, Ann Arbor, Mich., Nov. 1964 (Available from above address).

Elsasser, W. M., and M. F. Culbertson. "Atmospheric Radiation Tables," Meteorological Monographs, Vol. 4, No. 23, Aug. 1960, American Meteorological Society, Boston, 43 pp.

Hanel, R. A. and L. Chaney, "The Infrared Interferometer Spectrometer Experiment (IRIS): Vol. II-Meteorological Mission," Unpublished manuscript, 1965.

Hilleary, D. T., D. Q. Wark, and D. G. James. "An Experimental Determination of the Atmospheric Temperature Profile by Indirect Means," Nature, Vol. 205, No. 4970, Jan. 1965, pp. 489-491.

Houghton, J. T. "Meteorological Significance of Remote Measurements of Infrared Emission from Atmospheric Carbon Dioxide," Quarterly Journal of the Royal Meteorological Society, Vol. 87, No. 371, Jan. 1961.

King, J. I. F. "The Radiative Heat Transfer of Planet Earth," Scientific Uses of Earth Satellites, Second Rev. Ed., Ed. by J. A. Allen, University of Michigan Press, Ann Arbor, 1958, 316 pp.

King, J. I. F. "Meteorological Inferences from Satellite Radiometry. I," Journal of the Atmospheric Sciences, Vol. 20, No. 4, July 1963, pp. 245-250.

King, J. I. F. "Inversion by Slabs of Varying Thickness," Journal of the Atmospheric Sciences, Vol. 21, No. 3, May, 1964, pp. 324-326.

Kuhn, P. M. "Measured Effective Long-Wave Emissivity of Clouds," Monthly Weather Review, Oct.-Dec. 1963. pp. 635-640.

Meeks, M. L. and A. E. Lilly, "The Microwave Spectrum of Oxygen in the Earth's Atmosphere," Journal of Geophysical Research, Vol. 68, No. 6, March 1963, pp. 1986-1703.

Wark, D. Q. "On Indirect Temperature Soundings of the Stratosphere from Satellites," Journal of Geophysical Research, Vol. 66, No. 1, Jan. 1961. pp. 77-82.

Wark, D. Q. and H. E. Fleming. "Indirect Measurements of Atmospheric Temperature Profiles from Satellites," Monthly Weather Review, Vol. 94, No. 6, June, 1966.

Wark, D. Q. and D. M. Mercer. "Absorption in the Atmosphere by the Oxygen 'A' Band," Journal of Applied Optics, Vol. 4, July 1965, pp. 839-845.

Wark, D. Q., G. Yamamoto, and J. Lienesch. "Infrared Flux and Surface Temperature Determination from TIROS Radiometer Measurements," Meteorological Satellite Report No. 10, U.S. Department of Commerce, Weather Bureau, Washington, D.C., Aug. 1962 (Available from the Depository of the Library of Congress, Washington, D.C.).

Yamamoto, G. "Numerical Method for Estimating the Stratospheric Temperature Distribution from Satellite Measurements in the CO_2 Band," Journal of Meteorology, Vol. 18, No. 5, Oct. 1961, pp. 581-588.

Yamamoto, G., M. Tanaka, and K. Kamitani. "Radiative Transfer in Water Clouds in the 10-Micron Window Region," Journal of Atmospheric Sciences, Vol. 23, No. 3, May 1966, pp. 305-313.

Reprinted from JOURNAL OF APPLIED METEOROLOGY, Vol. 5, No. 5, October 1966, pp. 726–727
American Meteorological Society
Printed in U. S. A.

Note on the Relationship Between Total Precipitable Water and Surface Dew Point

W. L. SMITH
University of Wisconsin, Madison
17 March 1966 and 12 May 1966

1. Introduction

Recently Reitan (1963) achieved a correlation of 0.98 between mean monthly total precipitable water and mean monthly surface dew point from a total of 540 observations. He found that the line of regression relating these mean values was of the form

$$\ln U = A + Bt_d, \tag{1}$$

where U is precipitable water (cm), t_d is the dew point temperature (°F), $A=-0.981$ and $B=0.0341$. Reitan estimates the standard error from regression at 10 per cent. The above result prompted Bolsenga (1965) to follow the same procedure to determine the regressional relations between mean daily and hourly observations of total water vapor content and surface dew point. Although the correlations he estimates are lower (0.85 to 0.80 for the mean daily and hourly observations, respectively), he found that the same basic relationship given by Eq. (1) exists. Bolsenga, however, estimates the coefficients of Eq. (1) to be $A=-1.249$ and $B=0.0427$ for the mean daily observations, and $A=-1.288$ and $B=0.0384$ for the hourly observations. Estimates of explained variance reveal that about 96 per cent of the differences in total water vapor are related to differences in dew point for the mean monthly values, 72 per cent for mean daily values and 64 per cent for hourly values. Since a unique relationship between total water content and surface dew point depends on the variability of the moisture profile, the tendency towards lower correlations with decreasing time intervals is to be expected.

In this note, an equation is derived which is of the same form as that obtained statistically by Reitan and Bolsenga with the exception that the A coefficient is not a constant, but a variable which is clearly dependent upon the actual moisture profile. Climatic values of the moisture profile are obtained which will enable good estimates of the total water vapor content to be obtained from the surface dew point regardless of latitude or season.

2. Development

For most practical purposes, the relation between vapor pressure e and dew point may be given by the empirical formula of Tetens (1930),

$$e = E_0 \times 10^{(\alpha t_d - \beta)/(t_d + \gamma)}, \tag{2}$$

where $E_0=6108$ dyne cm^{-2}, $\alpha=7.5$, $\beta=238.1$F and $\gamma=395.1$F when t_d is expressed in °F. Since the surface mixing ratio w_0 is given to a good approximation by

$$w_0 = \epsilon \frac{e_0}{p_0}, \tag{3}$$

where p_0 is the pressure at the earth's surface and $\epsilon=0.622$, it follows from Tetens' relation that

$$w_0 = \frac{\epsilon E_0}{p_0} \times 10^{(\alpha t_d - \beta)/(t_d + \gamma)}. \tag{4}$$

Ordinarily the moisture content is greatest at the earth's surface and decreases to a value of zero at the top of the atmosphere. Regardless of the exact moisture profile, with the proper choice of a power λ for a given atmospheric situation, the average decrease of moisture through the entire atmospheric column may be described by the power law

$$w = w_0 \left(\frac{p}{p_0}\right)^{\lambda}. \tag{5}$$

From the definition of the vertical mean mixing ratio $\bar{w}$, it follows that

$$\bar{w} = \frac{1}{p_0} \int_0^{p_0} w_0 \left(\frac{p}{p_0}\right)^{\lambda} dp = \frac{w_0}{\lambda+1}. \tag{6}$$

Since it can be shown that the total precipitable water U is related to the mean mixing ratio by

$$U = \frac{p_0}{g} \bar{w},$$

where g is the acceleration of gravity, then

$$U = \frac{p_0 w_0}{g(\lambda+1)}. \tag{7}$$

Eq. (7) illustrates the relationship between the total water vapor content and surface moisture conditions for a particular moisture profile as described by λ.

Substituting (4) into (7) yields

$$U=\frac{\epsilon E_0}{g(\lambda+1)}\times 10^{(\alpha t_d-\beta)/(t_d+\gamma)}, \quad (8)$$

or

$$\ln U=\ln\left(\frac{\epsilon E_0}{g}\right)-\ln(\lambda+1)+\left(\frac{\alpha t_d-\beta}{t_d+\gamma}\right)\ln 10. \quad (9)$$

Considering the normal range of surface dew points and the magnitude of t_d with respect to the magnitude of γ, little error will result if the denominator $(t_d+\gamma)$ is assigned the mean value of 440F. Evaluation of Eq. (9) then yields

$$\ln U=[0.1133-\ln(\lambda+1)]+0.0393t_d, \quad (10)$$

which is of the same form as the regression equation obtained by Reitan and Bolsenga. In (10), however, the "A" coefficient is not necessarily a constant, but depends on the vertical distribution of moisture. It is interesting to note that B has very nearly the values obtained by Reitan and Bolsenga.

As indicated earlier from the results of Reitan and Bolsenga, the longer the time period over which the mean values of water vapor content and surface dew point are formed, the more unique the relation is between these two variables; or, as depicted by (10), the better the approximation becomes that the moisture profile is constant. The scatter about the statistically determined regression lines of Reitan and Bolsenga merely results from variations of λ.

3. Improvements

Table 1 illustrates the dependence of λ on latitude and season. These values of λ were obtained from the mean Northern Hemisphere soundings tabulated by London (1957). It should be noted that the Northern Hemisphere averages are derived by weighting each latitude band equally. For a given surface dew point, it follows from (10) that the percentage error resulting in an estimate of U from an incorrect estimate of λ is given by

$$\text{Error } (U)\equiv 100\frac{U-U}{U}=100\frac{\hat{\lambda}-\lambda}{\hat{\lambda}-1},$$

where U, λ are the true values and $\hat{U}$, $\hat{\lambda}$ are the estimated values. Since the "A" coefficients obtained by Reitan and Bolsenga imply $\hat{\lambda}$ values of about 2.0 and 3.0, respectively, it is evident from Table 1 that errors as large as 50 per cent may result even for mean monthly conditions. Hence it seems necessary to consider the latitudinal and seasonal dependence of λ when relating the surface dew point to the total water vapor content. This may now be done by utilizing Table 1 with Eq. (10). More characteristic relationships for individual stations could be obtained in a similar manner from tabulated values of λ for those stations. This type of information would indeed be a useful supplement to regions where few or no balloon soundings are available.

TABLE 1. Seasonal and latitudinal mean values of λ.

Season latitudinal zone (deg N)	Winter	Spring	Summer	Fall	Annual average
0–10	3.37	2.85	2.80	2.64	2.91
10–20	2.99	3.02	2.70	2.93	2.91
20–30	3.60	3.00	2.98	2.93	3.12
30–40	3.04	3.11	2.92	2.94	3.00
40–50	2.70	2.95	2.77	2.71	2.78
50–60	2.52	3.07	2.67	2.93	2.79
60–70	1.76	2.69	2.61	2.61	2.41
70–80	1.60	1.67	2.24	2.63	2.03
80–90	1.11	1.44	1.94	2.02	1.62
Northern Hemisphere average	2.52	2.64	2.62	2.70	2.61

Acknowledgments. This research was supported by the National Environmental Satellite Center of the Environmental Science Services Administration under Grant W.B.G. 25.

REFERENCES

Bolsenga, S. J., 1965: The relationship between total atmospheric water vapor and surface dew point on a mean daily and hourly basis. *J. Appl. Meteor.*, **4**, 430–432.

London, J., 1957: A study of the atmospheric heat balance. Final Report, Contract No. AF 18(122)-165, New York University, College of Engineering, Research Div., University Heights, New York, 99 pp.

Reitan, C. H., 1963: Surface dew point and water vapor aloft. *J. Appl. Meteor.*, **2**, 776–779.

Tetens, O., 1930: Über einige meteorologische Begriffe. *Z. Geophys.*, **6**, 297–309.

The Contribution of Infrared Cooling to the Vertical Motion Field and its Implication in Atmospheric Energetics

Ben R. Bullock, Lyle H. Horn, Donald R. Johnson

ABSTRACT:

The validity of the adiabatic assumption used in estimating vertical motion is examined by comparing the relative contributions due to adiabatic processes with the diabatic process of infrared cooling. Radiometersonde data are used to prepare vertical profiles of the adiabatic and infrared components of the vertical motion. These data are first filtered to reduce the effect of random errors. Although the adiabatic component of the vertical motion is usually much larger than the infrared component, the profiles indicate that the infrared component can be important in determining the total vertical motion. A comparison of the contribution of the infrared component in cloudy versus clear sky conditions shows this component to contribute more to downward vertical motion in clear air than in the cloudy situations. The consequences of this systematic variation in estimating energy conversions is discussed. In view of these results the effect of other diabatic processes is very briefly considered.

1. INTRODUCTION

In many studies the so-called adiabatic method, which involves the First Law of Thermodynamics and the adiabatic assumption, is used to obtain the field of vertical motion. Despite the necessity of the adiabatic assumption, this procedure for computing vertical motions (Haltiner and Martin, 1957) is widely used in meteorology, primarily because other techniques, such as the kinematic and vorticity methods require assumptions possibly as restrictive as the adiabatic assumption. A study by Shenk (1963), which in effect correlated vertical motion as calculated by the adiabatic method with a measure of cloud distribution estimated from satellite radiation measurements, produced a correlation coefficient of 0.77. While

Shenk studied the large-scale vertical motion field, Hansen and Thompson (1965) used TIROS cloud photographs and the vertical motion field obtained from both the kinematic and adiabatic methods to examine smaller scale variations in the vertical motion field. Although in general they obtained their best results using the kinematic method, they also concluded that when studying larger scale motions where data limitations may exist the adiabatic velocities are of more value.

In energy studies, an understanding of the circulation of the atmosphere requires a description of the vertical motion field through which the available potential energy of the atmosphere is converted into kinetic energy. The conversion process involves the sinking of relatively cold air and the rising of warm air, the magnitude of the conversion being proportional to the integral of the covariance of the departures from areal means of the vertical velocity and specific volume or temperature (Lorenz, 1955).

In several atmospheric energetics studies the adiabatic method has been used to estimate the conversion of available potential energy to kinetic energy (White and Nolan, 1960; Jensen, 1961). The importance of using accurate vertical velocity estimates in these conversion computations cannot be overemphasized, since the magnitude of kinetic energy production determines the intensity of the general circulation. Furthermore, an understanding of the mode of the atmosphere's circulation requires a determination of the scales and mechanism by which this conversion occurs. Wiin-Nielsen (1964) notes that use of adiabatic vertical velocities to obtain the conversion of available potential energy to kinetic energy can be misleading.

In any study employing adiabatic vertical velocities, the validity of the results depends critically upon the adiabatic assumption. For certain cases high in the atmosphere this assumption is not unrealistic. However, in other atmospheric regions, especially the lower and midtroposphere, the diabatic processes of absorption and emission of radiant energy, the release of latent heat, and sensible heat addition at the earth's surface tend to make estimates of the vertical motion field based on the adiabatic method less reliable. While latent heat release and sensible heat transfer are difficult to measure, radiational processes can be measured by devices such as the Suomi-Kuhn radiometersonde and satellites.

In view of the importance of an accurate determination for both energy studies and the possibility of inferring the large-scale vertical motion field from satellite data, the significance of one diabatic component—infrared radiation—upon adiabatic estimates of the field of vertical motion is investigated in this paper. Soundings of the infrared cooling made at Washington, D.C.; Montgomery, Alabama;

Green Bay, Wisconsin; International Falls, Minnesota, and Amarillo, Texas, selected from the periods 20-28 December 1960, and 7-18 January 1961, are used to estimate the contribution of this diabatic process to the field of vertical motion. Separate vertical profiles of the vertical motion associated with adiabatic processes and with the infrared component of the diabatic process are compared by using 1) a limited sample of polynomial filtered profiles, and 2) a larger but unfiltered sample of profiles. Because of the importance of vertical motion estimates in obtaining energy conversions, the effect of neglecting the diabatic processes is discussed in some detail.

2. BASIC EQUATIONS

Since the large-scale vertical motion field cannot be measured directly, it must be found through indirect methods. In this study the First Law of Thermodynamics is used in developing an expression for the vertical motion. This expression is divided into two parts, the one which is normally used in obtaining adiabatic estimates and another which gives the error introduced by neglecting diabatic processes. Using the notation from the List of Symbols, the First Law of Thermodynamics may be expressed as

$$\frac{dh}{dt} = c_p \frac{dT}{dt} - \alpha\omega \tag{1}$$

After expanding the total temperature derivative, the solution for the vertical velocity in constant pressure coordinates is

$$\omega = \frac{\frac{\partial T}{\partial t} + \vec{V} \cdot \vec{\nabla}_p T - \frac{1}{c_p}\frac{dh}{dt}}{\frac{\alpha}{c_p} - \frac{\partial T}{\partial p}} \tag{2}$$

Our discussion of vertical motion in this paper is based on the definition for vertical velocity in constant pressure coordinates and should not be confused with the vertical velocity, w, for cartesian coordinates.

Using Poisson's Equation and the Equation of State, equation (2) becomes

$$\omega = \frac{-\left(\frac{\partial T}{\partial t} + \vec{V} \cdot \vec{\nabla}_p T - \frac{1}{c_p}\frac{dh}{dt}\right)}{\left(\frac{p}{1000}\right)^{R_d/c_p} \frac{\partial \theta}{\partial p}} \tag{3}$$

Equation (3) represents the true vertical motion, and all adiabatic and diabatic processes must be known to obtain its value. For purposes of discussion the vertical motion may be thought of as consisting of two components, one associated with the adiabatic processes and the other associated with diabatic processes. The adiabatic portion of the vertical motion obtained by assuming $dh/dt = 0$ is

$$\omega_A = \frac{-\left(\frac{\partial T}{\partial t} + \vec{V} \cdot \vec{\nabla}_p T\right)}{\left(\frac{p}{1000}\right)^{R_d/c_p} \frac{\partial \theta}{\partial p}} \tag{4}$$

The diabatic component of the vertical motion obtained by subtracting equation (4) from equation (3) is

$$\omega_D = \frac{\frac{1}{c_p} \frac{dh}{dt}}{\left(\frac{p}{1000}\right)^{R_d/c_p} \frac{\partial \theta}{\partial p}} \tag{5}$$

Equation (4) is the usual expression for the adiabatic component of the vertical motion field, and equation (5), which represents the diabatic effect will for convenience be designated the "diabatic component" of the vertical motion field. In this study only the non-adiabatic heating component due to the field of terrestrial radiation is considered. Under steady-state conditions and horizontal isotropy for the field of infrared irradiance the heat addition per unit mass due to the infrared component is

$$\left(\frac{dh}{dt}\right)_I = g \frac{\partial F_n}{\partial p} \tag{6}$$

Thus the diabatic component of vertical motion due to the field of infrared irradiance is

$$\omega_I = \frac{\frac{g}{c_p} \frac{\partial F_n}{\partial p}}{\left(\frac{p}{1000}\right)^{R_d/c_p} \frac{\partial \theta}{\partial p}} \tag{7}$$

The adiabatic estimate of the vertical motion field is obtained using (4), and the infrared diabatic component is estimated by (7) from data provided by radiometersonde soundings (Suomi-Kuhn, 1958). In this study the importance of infrared processes is examined by comparing profiles of this diabatic component of the vertical motion field with profiles using the adiabatic assumption.

In the subsequent sections, filtering techniques are applied to a small sample of data to reduce the effects of random errors and small scale variations, thus improving the estimation accuracy of the vertical velocities. Because of the small size of this sample, a larger but unfiltered sample is also used.

3. COMPUTATIONAL PROCEDURES

3.1. Adiabatic estimates of vertical velocities. The calculation of adiabatic vertical velocities by equation (4) requires estimates of the local temperature tendency, horizontal temperature advection, and the stability measure. An inherent problem in calculating adiabatic vertical velocities using synoptic data is that the local temperature tendency is a time averaged determination while the horizontal advection by the geostrophic wind field is a spatially determined quantity at a given time (Panofsky, 1951). The infrared component is calculated from data taken at the same time as that used in computing the advection term in the adiabatic velocity equation. In order to obtain diabatic and adiabatic profiles which may be considered representative for the same time, the local temperature tendency has been determined from observations taken 24 hours apart while the advection term of the adiabatic equation and infrared component computation were made from data taken at the midpoint of the 24 hour period. For compatibility we assume that the 24 hour temperature tendency is representative of the actual tendency at the midpoint.

The above assumption seems reasonable because the free atmosphere temperature time series tends to be a smooth function whose principal variation is associated with large scales of motion with periods of several days between adjacent relative temperature maxima and minima. For this scale of variation, one would normally expect that a second order Taylor's series expansion about the midpoint time t_0 would provide a valid description of the temperature in the 24-hour interval from t_0 - 12 hours to t_0 + 12 hours. If this condition is satisfied, then the finite estimate of the 24-hour time average temperature tendency should be a valid estimate for the local temperature tendency at the time t_0.

In this study the horizontal temperature advection is determined through the thermal wind relationship. This allows the advection computation to be made solely from the data for a single station and thus avoids the problem of obtaining a geostrophic wind determination from the large-scale pressure pattern. In pressure coordinates and under the assumption that the acceleration and frictional force are constant with height, the vector equation for the vertical wind shear in pressure coordinates is

$$\frac{\partial \vec{V}_h}{\partial p} = -\frac{R_d}{fp}\left(\vec{k} \times \vec{\nabla}_p T\right)$$

A rearrangement and scalar multiplication of both sides by $\vec{V}_h$ yields the horizontal temperature advection

$$\vec{V}_h \cdot \vec{\nabla}_p T = \frac{fp}{R_d}\left(v\frac{\partial u}{\partial p} - u\frac{\partial v}{\partial p}\right) \qquad (8)$$

The accuracy of the temperature advection computed with equation (8) depends upon the accuracy of the method used to evaluate u, v, $\frac{\partial u}{\partial p}$, and $\frac{\partial v}{\partial p}$. Since the u and v wind components at each pressure level contain random errors plus small-scale wind variations, serious errors in the estimation of these quantities result if a method is not used to reduce the influence of random errors and small-scale variations, both of which are essentially noise superimposed upon the synoptic scale temperature variations.

One way of reducing the effect of this noise is to use least-squares approximating polynomials which filter a portion of the random errors and small-scale variations in the wind field. Approximating polynomials (Hildebrand, 1956) can be used whenever the basic observations to be filtered are discrete measurements of a smooth true function. The advantage of using least-square approximating polynomials is that an exact fit to the basic data is avoided. An exact fit requires the estimated function to pass through each data point, thus oscillating about the true function. On the other hand, approximating polynomials supply a better value of the smooth true function by removing the effects of random errors and small-scale wind variations.

In a portion of this study the u and v component profiles are filtered by fitting a second-degree polynomial to five adjacent observations which are vertically spaced at 50mb intervals. Pressure is used as the independent variable for filtering. The resulting polynomials, of the form $\hat{u} = u(p)$ and $\hat{v} = v(p)$, are then differentiated with respect to pressure and a set of filtered estimates $\partial\hat{u}/\partial p$ and $\partial\hat{v}/\partial p$ obtained at the midpoint of the five observations. The next set of filtered estimates are made by adding a new observation adjacent to the upper pressure level and deleting the observation at the lower pressure level and then predicting the new mid-observation. After obtaining values of $\hat{u}$, $\hat{v}$, $\partial\hat{u}/\partial p$, and $\partial\hat{v}/\partial p$ at all levels from 850 mb to 200 mb at 50 mb increments, filtered estimates of the horizontal temperature advection are computed using equation (8).

Figure 1, which presents vertical profiles of the raw and filtered values of the u-component of the wind at Washington, D.C. at 00z December 22, 1960, clearly illustrates the filtering effect of the

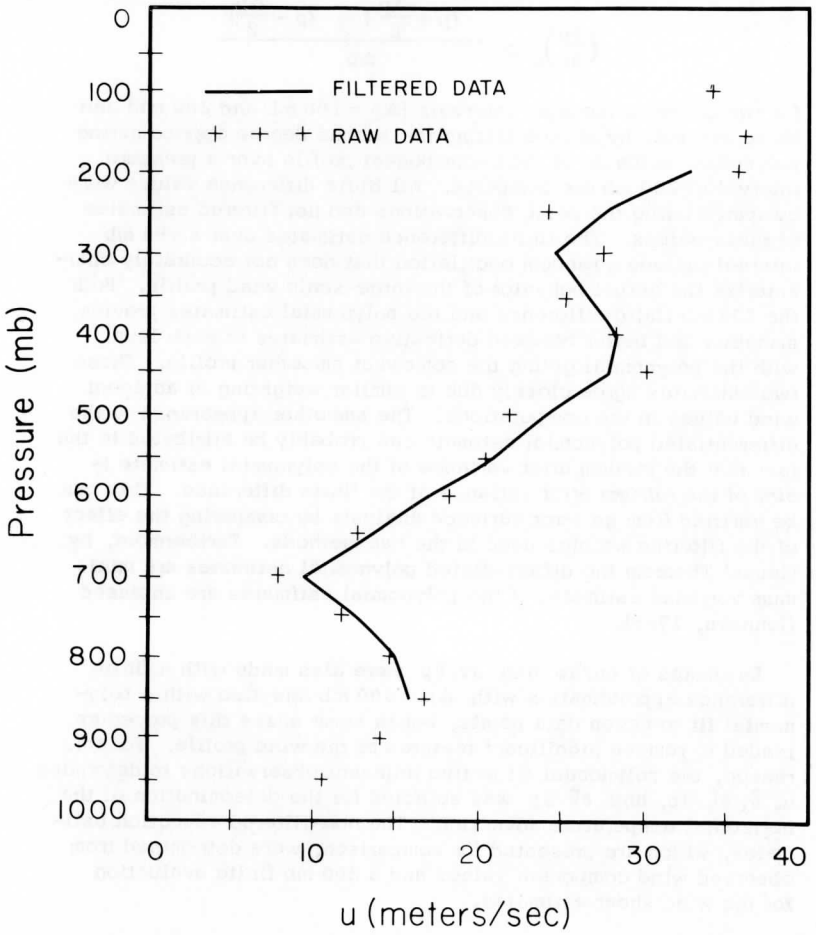

Fig. 1. Comparison of raw and filtered values of the eastward component of the wind at Washington, D.C., on 22 December 1960, 00Z.

least-squares approximating polynomials. In Figure 2 the estimates of $\partial u/\partial p$ computed by a finite difference approximation given by

$$\left(\frac{\partial u}{\partial p}\right)_p \simeq \frac{U_{(p+\frac{\Delta p}{2})} - U_{(p-\frac{\Delta p}{2})}}{\Delta p}$$

for two different pressure intervals (Δp = 100 mb and 200 mb) and those obtained by differentiating the second degree approximating polynomial estimate of the u-component profile over a pressure interval of 200 mb are compared. All finite difference values were computed using the basic observations and not filtered estimates of these values. The finite difference estimates over a 100 mb interval include a random oscillation that does not accurately characterize the actual behavior of the large-scale wind profile. Both the 200 mb finite difference and the polynomial estimates provide smoother and better behaved derivative estimates at each level, with the polynomial giving the somewhat smoother profile. These two estimates agree closely due to similar weighting of adjacent wind values in the computations. The smoother appearance of the differentiated polynomial estimate can probably be attributed to the fact that the random error variance of the polynomial estimate is 80% of the random error variance of the finite difference. This can be verified from an error variance analysis by comparing the effect of the filtering weights used in the two methods. Furthermore, by Gauss' Theorem the differentiated polynomial estimates are minimum variance estimates if the polynomial estimates are unbiased (Johnson, 1965).

Estimates of $\partial u/\partial p$ and $\partial v/\partial p$ were also made with a finite difference approximation with Δp = 300 mb and also with a polynomial fit to seven data points, but in some cases this procedure tended to remove significant features of the wind profile. For this reason, the polynomial fit to five adjacent observations to determine $\hat{u}$, $\hat{v}$, $\partial\hat{u}/\partial p$, and $\partial\hat{v}/\partial p$ was selected for the determination of the horizontal temperature advection. The non-filtered advection estimates, which are presented for comparison, were determined from observed wind component values and a 200 mb finite evaluation for the wind shear estimates.

The stability measure was also computed by differentiating the second degree polynomial fit of potential temperature with respect to pressure and, for comparison, by a finite difference approximation over a 200 mb layer. Values obtained by these methods agreed very well with few exceptions. In this data sample the improvement due to filtering the stability measure was not as striking as anticipated due to the fact that the static stability of the data for the middle latitude winter troposphere is large. In tropical regions

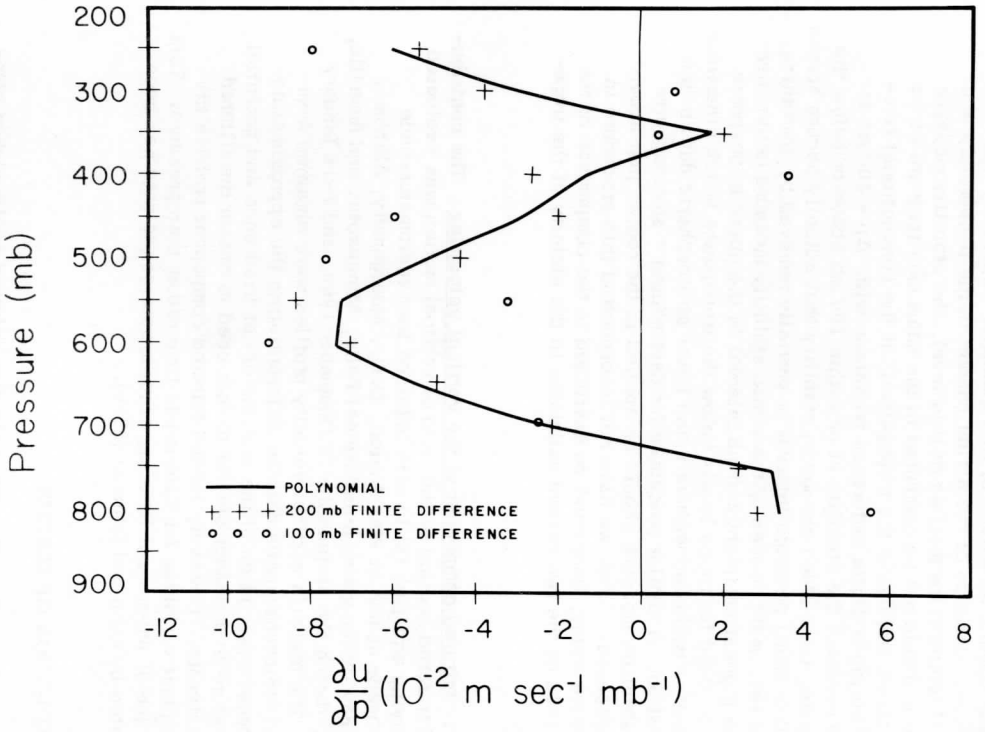

Fig. 2. Comparison of filtered and finite difference estimates of wind shear for the profile in Figure 1.

and summer conditions where the tropospheric lapse rate approaches the dry adiabatic, filtered estimates of the stability measure would provide a significant improvement. Included in Figures 3, 4, 5 and 6, which are discussed in the next section, are profiles of the filtered values of the stability measure. It is necessary to exercise caution in computing values of this quantity, especially near the tropopause. Because of the abrupt change in the temperature and potential temperature profiles at this level, the stability measure estimates should not be computed in the same way they are at the levels above and below the tropopause. If the conventional five-point filtering or finite difference technique with $\Delta p = 200$ mb is used to evaluate the stability at or within 100 mb above or below the tropopause, the sudden change in stability that actually occurs across this rather small pressure interval is partially removed by smoothing. For this reason the values of the static stability measure determined from the highest complete 200 mb interval in the upper troposphere should be used for those levels below the tropopause which otherwise could not be computed without using lower stratospheric data in the computation. A similar procedure for determining a stratospheric static stability measure should be applied in the region just above the tropopause. Since we have not incorporated this procedure in our present study, care must be exercised in the comparison of the magnitudes of the two biased estimates in the vicinity of the tropopause.

3.2. Infrared component of the vertical velocities. The contribution of infrared cooling to the field of vertical motion was evaluated by applying equation (6) to data obtained from radiometersonde flights made at 00Z at Washington, D.C.; Montgomery, Alabama; Green Bay, Wisconsin; International Falls, Minnesota; and Amarillo, Texas, during the periods 20-28 December 1960, and 7-18 January 1961. The diabatic vertical velocity profiles were obtained from filtered radiometersonde data by differentiating the approximating polynomial description of the profiles of net irradiance and potential temperature in a manner similar to that used to obtain the filtered wind estimate. However, for the infrared component profiles the independent variables for filtering is time rather than pressure. This technique of polynomial filtering of radiometersonde data has been presented by Kuhn and Johnson (1966).

4. DISCUSSION OF RESULTS

In this study the effect of neglecting infrared cooling when computing adiabatic vertical motions is considered by 1) comparing individual profiles of the adiabatic component obtained from filtered data with the infrared component for clear and cloudy regimes,

2) employing a synoptic case study of the time variation of the adiabatic and infrared profiles, and 3) comparing mean profiles of the infrared component with mean profiles of the adiabatic component obtained from a relatively large sample of unfiltered data, also for clear and cloudy conditions. Furthermore, because of the importance of the vertical motion field in energy studies, the implications of neglecting diabatic processes in energy conversions is discussed in a subsequent section.

Before comparing the adiabatic and diabatic components of the vertical velocity in clear and cloudy regions it may be well to compare the effect of finite difference and filtering techniques in estimating the adiabatic vertical velocities. Figure 3 presents one example of the vertical velocity profiles in a clear atmosphere. Profiles of adiabatic vertical velocity values obtained by use of filtered and non-filtered estimates of the horizontal temperature advection and stability measure estimates are shown for comparison. To illustrate the effect of the pressure interval used in finite difference evaluations of the temperature advection and stability measure in the determination of the adiabatic vertical velocity profiles, non-filtered estimates of the adiabatic vertical velocities are shown for two cases, Δp = 100 mb and Δp = 200 mb. In Figure 3 the 100 mb interval estimates portray a profile of adiabatic vertical motion that is not characteristic of large-scale atmospheric motions. The extreme oscillations in the velocity profile very likely reflect the presence of small-scale variations and random errors in the wind and temperature data. If a 50 mb interval is used, we would expect the resulting vertical velocity profiles to exhibit an even more pronounced oscillatory behavior.

Comparison of the 200 mb nonfiltered estimates and the filtered estimates reveals good agreement; however, in this example, the filtered profile is somewhat smoother than the nonfiltered one and displaces the region of maximum adiabatic vertical motion upwards by about 50 mb.

4.1. Individual clear and cloudy sky profiles of adiabatic and infrared components of vertical motion. In addition to the adiabatic profiles of vertical motion, Figure 3 also presents the profile of the infrared component values for this clear sky case. In this instance the 200 mb filtered and nonfiltered estimates of the adiabatic vertical velocities agree well with our concept of vertical motion in a clear atmosphere, with positive values of ω_A throughout most of the troposphere. Likewise, the infrared component, though small, is predominantly positive.

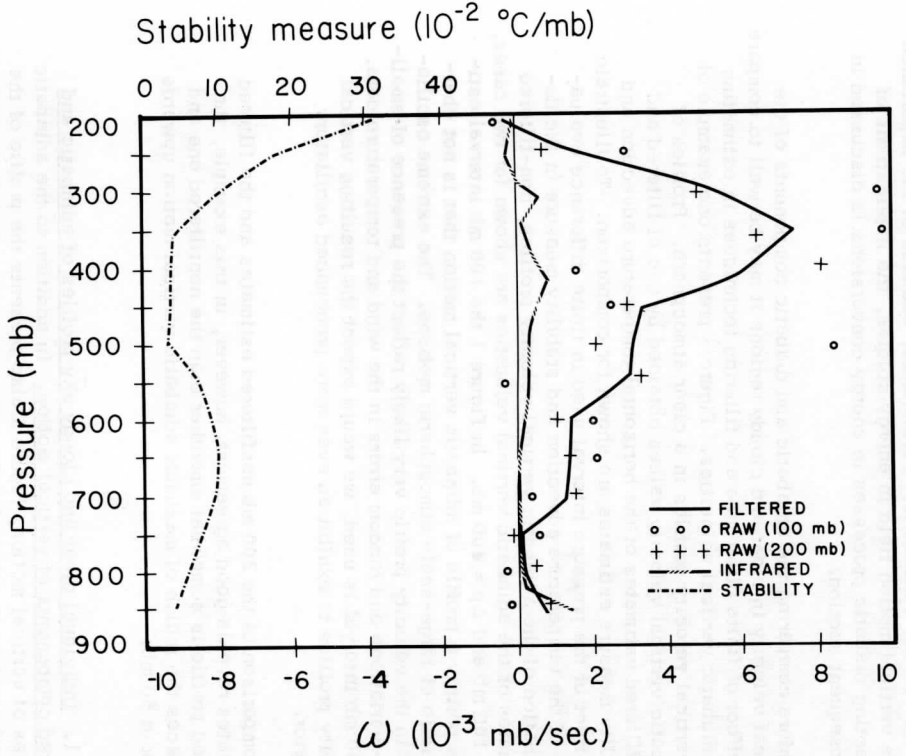

Fig. 3. Clear sky profiles of adiabatic and infrared components of vertical motion at Washington, D.C., on 20 December 1960, 00Z.

Unfortunately, not all vertical motion profiles from clear sky cases are as consistent as that presented in Figure 3. For example, Figure 4 shows a reasonable infrared component profile, but adiabatic profiles that display negative values of ω_A through a portion of the middle troposphere. The fact that no cloud cover was observed in this case could be attributed to a number of reasons. Cloud formation is not instantaneous but requires some finite time depending upon the initial degree of saturation. In support of the validity of this reasoning is the observation by Hansen and Thompson (1965) of a time lag between cloud formation as observed by TIROS photographs and the initiation of an upward vertical motion field as determined by the kinematic technique. In some situations, but not necessarily this particular clear case, the neglect of diabatic effects lead to erroneous estimates of vertical motion. And finally the possibility exists that errors were present in the data used to obtain the adiabatic estimates.

The infrared component was largest, as expected, in the presence of clouds. Figure 5 shows the vertical velocity profiles for Green Bay, Wisconsin, on an evening with an 0.8 cirrostratus overcast. In this case the adiabatic vertical velocity maximum near 350 mb corresponds closely to the cloud location while the maximum infrared component occurred in the vicinity of the cloud top. The adiabatic vertical velocity profiles agree fairly well with expected upward motion in a cloudy situation, except in the region between 450 mb and 550 mb where downward motion is indicated just below the cloud. The cloud top coincides very closely with the tropopause, which explains the sudden decrease in adiabatic vertical velocities to zero in the region above.

A second example of vertical velocity profiles for a cirrostratus overcast condition is presented in Figure 6. In this case, the adiabatic contributions to the total vertical motion is positive almost everywhere below the cloud, which appears inconsistent with the maintenance of a cloud.

4.2. Case study. To illustrate the temporal variations that occurred in the adiabatic and infrared components of the vertical motion profiles with changes in the synoptic weather pattern, the four day period 12-15 January 1961, at Washington, D.C., is considered. During the first two days of the period, skies at Washington were clear as high pressure dominated the eastern United States. However, on January 13 a low pressure area that had formed off the Texas Gulf coast was just south of New Orleans and moving northeast at about 15 knots. There was a cold core low aloft to 300 mb over central Texas to the west of the surface depression. By 06Z on January 14 the low pressure center was located just west of Tallahassee, Florida, with a cold front along the western Florida coast and a warm

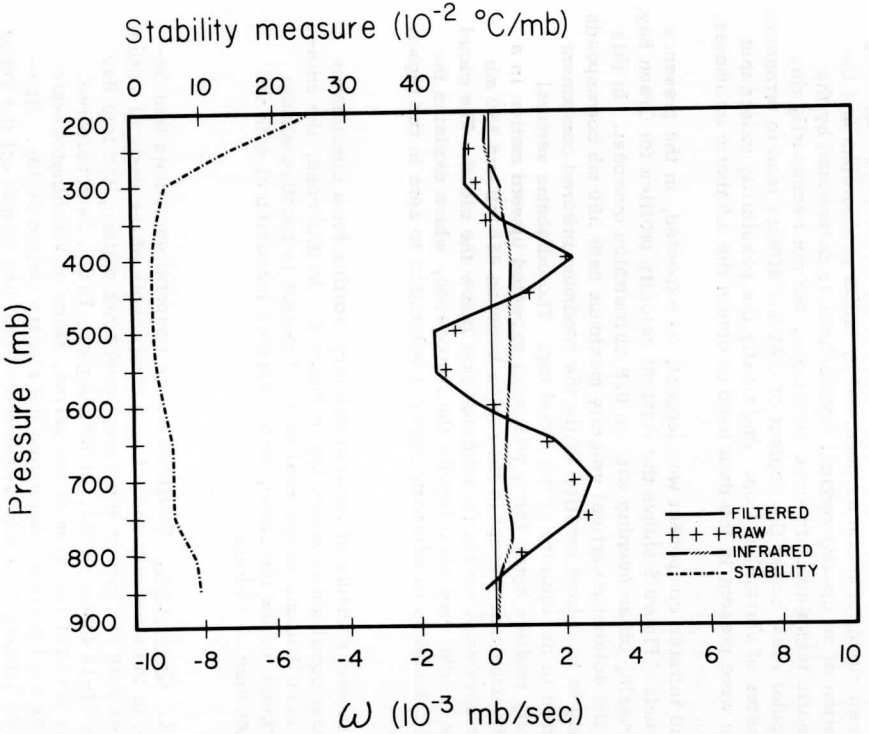

Fig. 4. Clear sky profiles of adiabatic and infrared components of vertical motion at Washington, D.C., on 26 December 1960, 00Z.

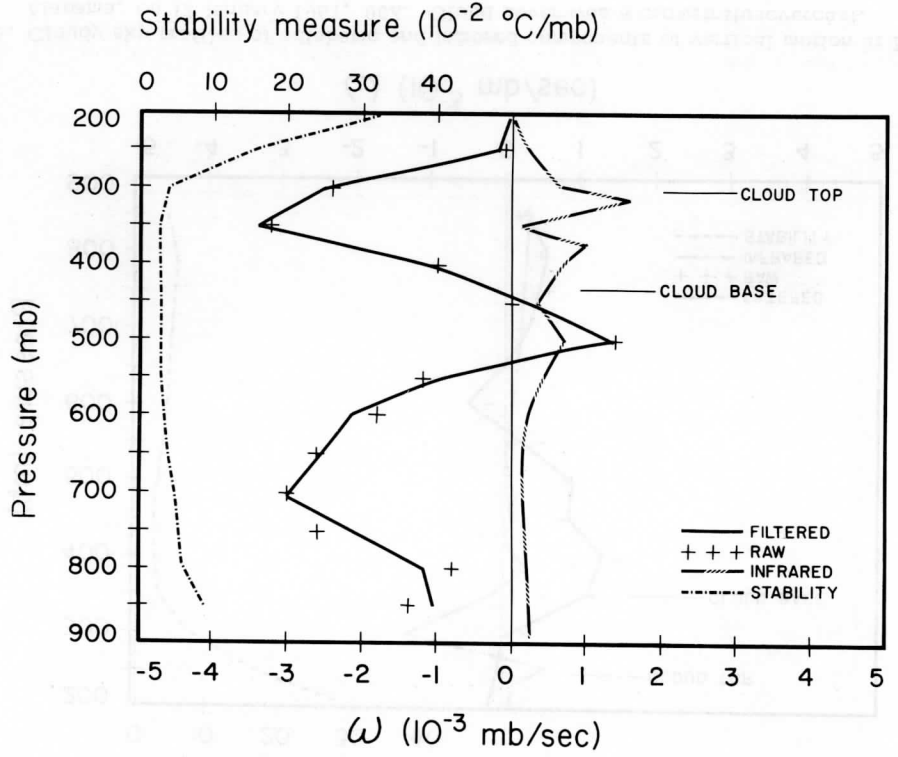

Fig. 5. Cloudy sky profiles of adiabatic and infrared components of vertical motion at Green Bay, Wisconsin, on 17 January 1961, 00Z. Cloud cover was reported as 0.8 cirrostratus.

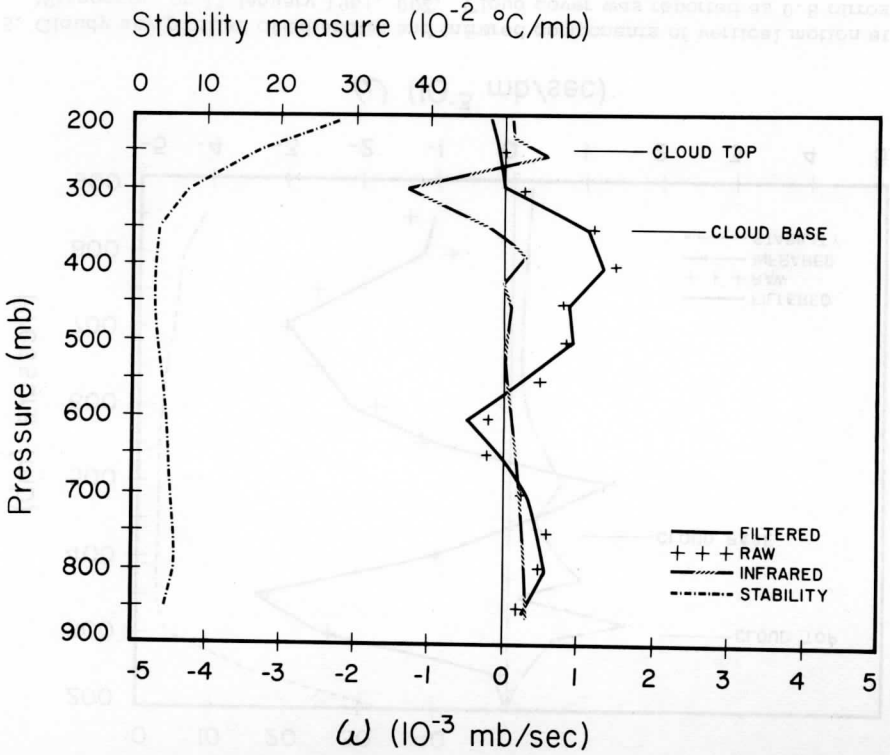

Fig. 6. Cloudy sky profiles of adiabatic and infrared components of vertical motion at Montgomery, Alabama, on 12 January 1961, 00Z. Cloud cover was a cirrostratusovercast.

front through southern Georgia into the Atlantic. At 00Z on January 14 there was scattered cirrus and at 06Z scattered stratocumulus present over Washington. On January 15 there was a nimbostratus overcast with continuous rain as the low pressure center moved southeast of Washington on a northeasterly course.

Figure 7 shows the variation with time of the adiabatic vertical velocities at four selected pressure levels. During the first two days of the period the adiabatic method indicated general subsidence at all levels except 500 mb. The large negative value of ω_A on January 12 probably results from an observational error. By 12Z on January 14 the adiabatic velocities indicated generally upward motion, and by the end of the fourth day the strength of the upward motion was decreasing at most levels.

Figure 8 presents the infrared component profiles at 00Z for each day of the period. The first two days show profiles typical of clear skies, while the third day shows some effect of cirrus with bases located at about 250 mb. Examination of the profile for 15 January shows a more pronounced effect with the top of the highest cloud layer to be about 300 mb. Apparently the effective emissivity of the cirrus layer on 15 January was much greater than on 14 January. The lack of variation in the profile below 550 mb indicates nearly radiational equilibrium below this level.

The adiabatic vertical velocity estimates in this case study showed generally good agreement with our concept of the vertical motion field for the synoptic pattern, a result that was not true in all cases. Also, the diabatic component corresponded well with cloud conditions and demonstrated its importance in the cloudy regions.

4.3. Mean clear and cloudy profiles. Although filtered profiles of adiabatic velocities were used for comparison with the infrared components in individual cases, it was not possible, because of the limited number of cases, to obtain mean profiles which were significant. The limited number of filtered profiles resulted from the fact that data at 50 mb increments, which were necessary for application of the filtering technique were available for only some cases. Consequently mean profiles of infrared and unfiltered adiabatic velocities were prepared from a relatively large sample of data obtained at standard levels. Since the interval between standard levels ranges from 150 to 200 mb, filtering offers little significant advantage in the construction of a mean profile. The validity of this result is confirmed by the comparison of adiabatic vertical velocity profiles obtained from raw data at 200 mb increments with filtered data at 50 mb increments in Figure 3.

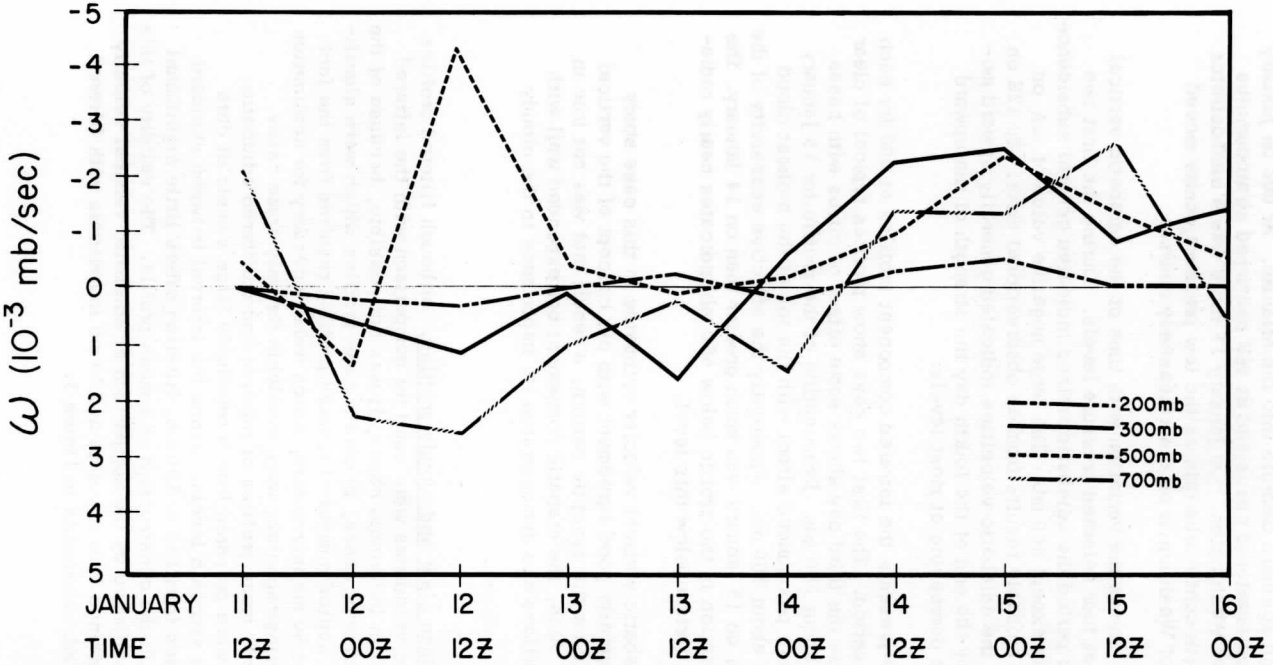

Fig. 7. Time cross section of the adiabatic component of vertical motion at four selected levels at Washington, D.C., for the period 11 - 16 January 1961.

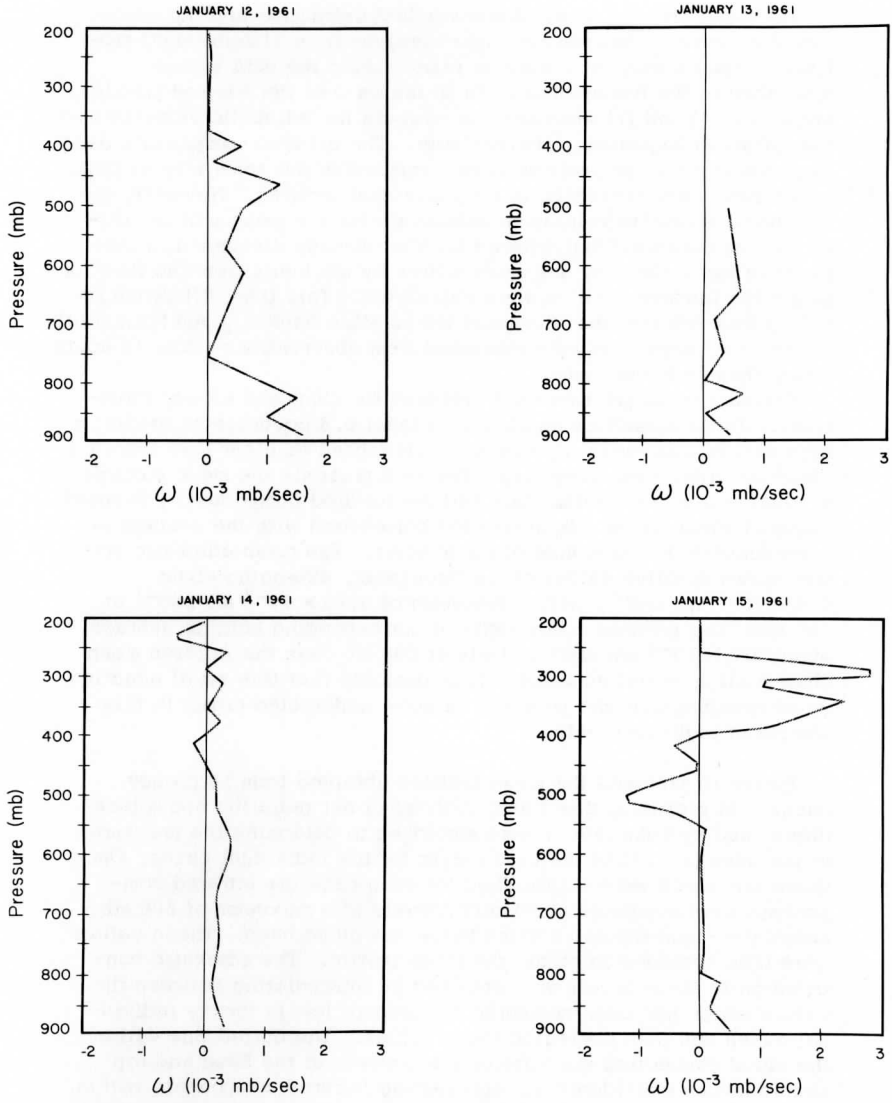

Fig. 8. Vertical profiles of the infrared component of vertical motion at 00Z for four days of the case study.

The mean profiles of adiabatic vertical velocities and the corresponding infrared components were obtained from 31 individual profiles computed from observations taken during the data period described in the introduction. As in the case of the filtered profiles, equations (4) and (7) were used to compute the adiabatic velocities and the infrared components, respectively. The infrared components used to compute the mean profiles were computed in the same way as those which have been presented in the individual profiles. However, the unfiltered adiabatic velocities used to obtain the mean profiles differed from the individual filtered profiles already discussed in that the time for which they are valid differs by six hours from the time for which the infrared profiles were calculated. This time difference resulted from the fact that the local temperature tendency and horizontal temperature advection were computed from observations taken 12 hours rather than 24 hours apart.

Separate mean profiles were prepared for clear and cloudy situations. To be classified as cloudy at least 0.8 coverage of middle or high clouds was required, and to be classified as clear less than 0.1 cloud coverage was necessary. Figure 9 presents the mean profiles of adiabatic vertical velocities and the infrared components computed using 21 clear cases. Both profiles correspond with the concept of subsidence in the presence of clear skies. The mean adiabatic profile shows positive values of ω_A throughout, averaging about 0.4×10^{-3} mb sec^{-1}, with a maximum of 0.75×10^{-3} mb sec^{-1} at 500 mb. The infrared components at corresponding heights average about 0.2×10^{-3} mb sec^{-1}. Only at 200 mb does the infrared mean show a slight negative value. It is possible that this small negative value resulted from the presence of some undetected cirrus in this sample of night time data.

Figure 10 presents the mean profiles obtained from 10 cloudy cases. In preparing this figure profiles of net radiation and a technique used by Kuhn (1966) were employed to determine the pressures at the base and top of the cloud layer for the individual cases. Once these pressures were established for each case the infrared components were computed at 50 mb intervals to a maximum of 200 mb above the cloud top and 200 mb below the cloud base. These values were then averaged to obtain the mean profile. The adiabatic contribution at these levels was obtained by interpolating between the values which had been computed at standard levels for the individual cases and then averaging those values. The dotted line within the cloud connecting the infrared components at the base and top should not be considered as representing infrared components within the cloud, since most of the cloud interior is in radiation equilibrium.

It should be noted that the relatively large negative value of ω_I at the mean cloud base and large positive value at the top are mainly due to a net absorption of infrared radiation at the base and emission

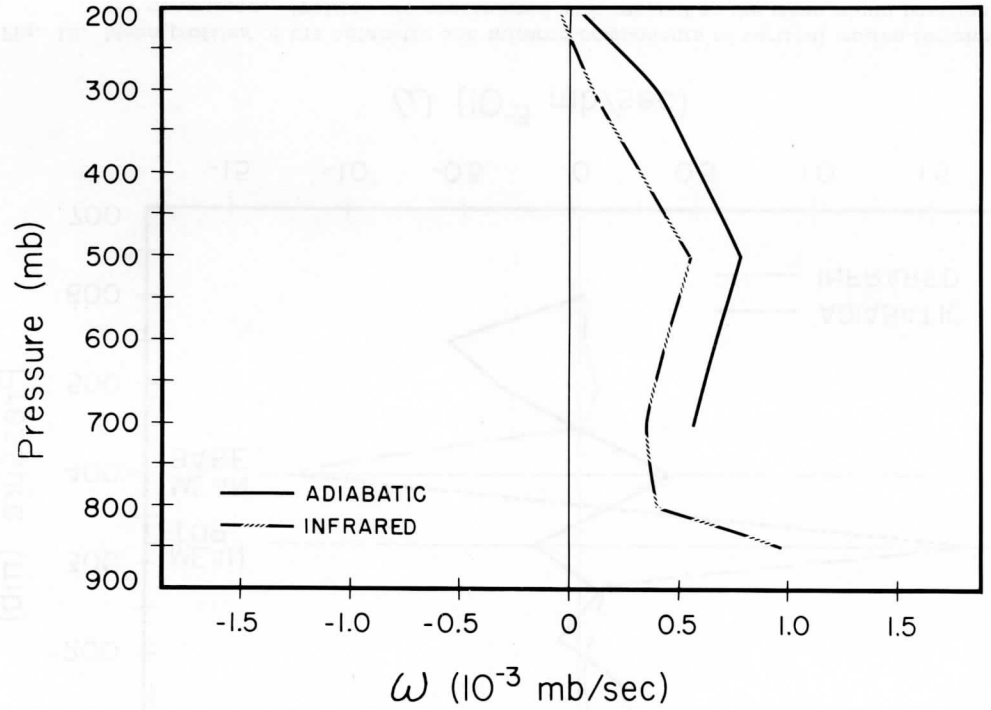

Fig. 9. Mean profiles of the adiabatic and infrared components of vertical motion for clear sky conditions. Compiled from 21 cases.

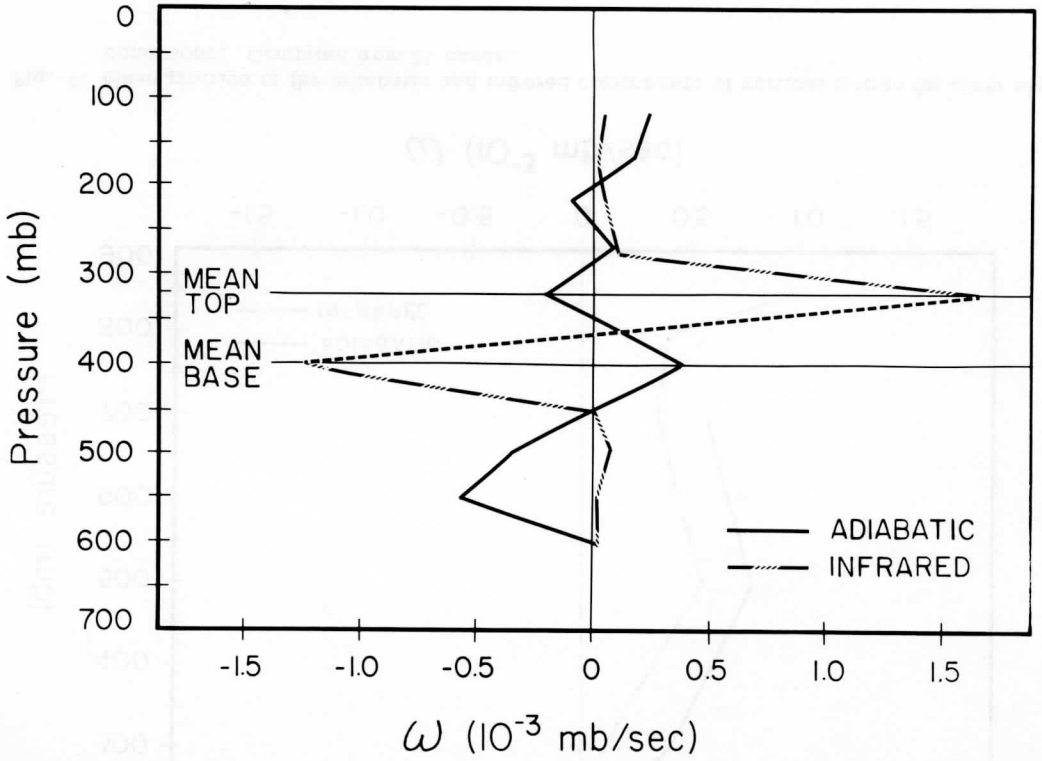

Fig. 10. Mean profiles of the adiabatic and infrared components of vertical motion for cloudy sky conditions. Profiles are constructed with respect to the mean cloud position of the 10 cases used.

at the top and are not representative of large scale vertical motion. However, these radiation processes are important in enhancing the small-scale turbulent motion in the clouds. The heating at the base and cooling at the top decreases the static stability within the cloud and consequently may lead to turbulent mixing and an increased upward heat transfer. Möller (1951) estimated that in a cloud 0.5 km thick at an elevation of 2 km only 45 minutes would be required to increase the lapse rate from isothermal to 0.5°C/100m, while in a cloud of the same thickness at an elevation of 5 km only 20 minutes would be needed to produce the same change. Möller assumed that no convective transfer of heat occurred during the destabilization process.

Although the infrared processes are important in clouds, the contribution of latent heat to vertical motions can be more significant. Immediately beneath a precipitating cloud layer the evaporating precipitation causes cooling, which may offset any infrared warming (and negative values of ω_I), but at lower levels the evaporation may reinforce any small positive values of ω_I. At the cloud base latent heat release due to condensation gives a negative contribution to the total vertical motion. At the cloud top there can be both condensation and evaporation of moisture. The condensation is the result of ascending motion, while evaporation results because of turbulent mixing and subsequent entrainment of dryer air from above. Whether heating or cooling is occurring at the cloud top depends upon which process is predominant.

Although the diabatic component of vertical motion in the vicinity of cloud top and base must be neglected when considering the large-scale vertical motion field, an examination of Figures 9 and 10 shows an important difference in the diabatic component profiles which are representative of large scale atmospheric processes. Infrared cooling beneath an extensive cloud layer is typically less than in clear conditions. For example, the average value of the infrared component of vertical motion in the mean cloudy profile (Fig. 10) between 450 and 600 mb is very close to zero, while the average value of this component in the mean clear profile (Fig. 9) in the same pressure interval is approximately 0.4×10^{-3} mb/sec.

5. CONSEQUENCE IN ENERGY CONVERSION ESTIMATES

Although the primary purpose of our study is to compare the infrared component of vertical motion with adiabatic vertical velocities to determine their importance, it is also important to consider the significance of these results in atmospheric energy studies. In this study the contribution of infrared cooling to the total vertical motion field was usually positive, but much more so in clear areas than in regions with middle or high clouds. Since growing and organized

weather disturbances are now recognized as major sites of the conversion of potential to kinetic energy in the middle latitudes (Starr, 1958), it is important to consider the magnitude of the bias error resulting from the use of adiabatic velocities in estimating the production of kinetic energy by the $\omega\alpha$ integral (Wiin-Nielsen, 1964). In troughs associated with growing and organized disturbances, cloudy areas tend to be associated with the warmer air to the east and clear areas with the colder air in and to the west of the mid-tropospheric trough. Since the infrared component of vertical motion tends to be in phase with the adiabatic vertical motion, the actual conversion will tend to be underestimated if the infrared component is neglected. To show how our results can be used to estimate that portion of the bias error due to the neglect of infrared radiation, consider the following development.

The general expression for the conversion of eddy available potential energy to eddy kinetic energy is

$$C(P,K) = -\int \omega' \alpha' dm \tag{9}$$

where m is the mass of the entire atmosphere and $( )'$ denotes deviations from a latitudinal mean on a pressure surface. The true but unknown eddy conversion, indicated by asterisks, is

$$C^*(P,K) = -\int \omega'^* \alpha'^* dm \tag{10}$$

Since the total vertical motion field is given by the sum of adiabatic and diabatic portions, equation (10) may be written as

$$C^*(P,K) = -\int (\omega_A'^* + \omega_D'^*)\alpha'^* dm \tag{11}$$

If we assume that the estimates of the specific volume and the adiabatic vertical velocity are unbiased and their random observational errors uncorrelated, the expected value of conversion estimates using the adiabatic assumption is

$$E[C(P,K)] = -\int \omega_A'^* \alpha'^* \, dm = C^*(P,K) - \delta \tag{12}$$

where

$$\delta = -\int \omega_D'^* \alpha'^* \, dm \tag{13}$$

Equations (12) and (13) show that the bias error δ is given by the covariance of the diabatic component and the specific volume. The diabatic component of the vertical velocity is

$$\omega_D = \omega_S + \omega_I + \omega_L + \omega_C + \omega_F \tag{14}$$

where:

ω_S = direct solar absorption

ω_I = emission of infrared energy

ω_L = release of latent heat

ω_C = sensible heat addition by conduction at the earth's interface

ω_F = internal heat addition due to frictional dissipation of kinetic energy

In the developing and organized stages of the weather producing disturbance the diabatic components of the release of latent heat, infrared cooling, and solar absorption are in phase with the adiabatic vertical motion and the specific volume fields. The component of sensible heat addition at the earth's surface is opposite in phase to the fields of vertical motion and the specific volume, since the coldest air at the surface will be heated more than the warm air. The frictional component is unimportant, for there should be little covariance between specific volume or ω and the frictional dissipation of the horizontal kinetic energy. Thus, the systematic bias error due to the neglect of the four heating components is

$$\delta = - \int (\omega_S'^* + \omega_I'^* + \omega_L'^* + \omega_C'^*)\alpha'^* \, dm \qquad (15)$$

where the first three left terms of the integral tend to be positive causing the adiabatic conversion estimates to be low while the last term tends to be negative causing the adiabatic conversion estimates to be high. Our results, although tentative, allow a quantitative estimate for the infrared component. The results shown in Figures 9 and 10 indicate that the infrared diabatic component may be expressed as

$$\omega_I' = b_I \omega_A' \qquad (16)$$

where the value of b_I lies at least between 0.1 and 0.2, and is possibly greater. For the regions of the quasi-geostrophic planetary waves (i.e., those without embedded smaller, organized disturbances) for which the adiabatic assumption is valid or for unorganized scales in which there is probably no systematic relation between the diabatic component of vertical motion and the adiabatic vertical velocities, b_I may be set to zero without inducing estimation errors in the conversion integral. Under these approximations the infrared bias error component in adiabatic vertical velocities is

$$\delta_I = - \{ \int b_{I_1} \omega_{A_1}'^* \alpha_1'^* \, dm_1 + \int b_{I_2} \omega_{A_2}'^* \alpha_2'^* \, dm_2 \} \qquad (17)$$

where the subscript one denotes values from atmospheric regions possessing organized disturbances, and the subscript two denotes values associated with quasi-geostrophic scales and unorganized circulations. If one assumes that 50 percent of the estimated conversion by the adiabatic method occurs in organized disturbances of the smaller synoptic scales and 50 percent in the larger planetary scale without an organized heating field in which b_{I_2} is zero, the bias infrared error component related to the expected value of adiabatic estimates is

$$\delta_I = \frac{b_{I_1}}{2} E[C(P,K)] \qquad 0.1 \leq b_{I_1} \leq 0.2 \tag{18}$$

thus estimates of the conversion of potential energy are underestimated and the actual adiabatic estimates should be adjusted upward by 5 to 10 percent to remove the infrared component bias and to achieve better estimates of the true conversion.

Undoubtedly there is a similar significant and more striking bias error due to the neglect of the effects of latent heat in the precipitating regions of the organized disturbance; however, the region of the intense organized disturbances in which there is net condensation with a subsequent release of latent heat is considerably less than the regions over which the infrared bias is present. The results obtained by Danard (1964) for ω_A and ω_L indicate that a possible range for b_L is from 1.0 to 1.5. Thus it is possible that the actual adiabatic estimates should be adjusted upward by 50 to 75 percent to remove the bias from the neglect of latent heat release.

With respect to the bias conversion error introduced by the neglect of the effects of sensible heat addition at the earth's interface, the systematic bias error, δ_C, should be negative. Sensible heat addition at the earth's interface will always be larger in the colder air than in the warmer air. This is particularly true in the winter when cold continental air flows off the eastern portions of both the Asian and North American continents. The effect of neglecting the component of the vertical motion associated with sensible heating and use of the adiabatic vertical component is to overestimate the magnitude of the downward vertical motion. In the boundary layer the magnitude of the true vertical motion should be small, and in the presence of strong sensible heating of the cold air the adiabatic component, which is a large positive value, may be nearly balanced by a large negative diabatic component. Thus the sign of b_C, corresponding to the definition of b_I, is probably negative and δ_C is also negative. Although we are unable to estimate the magnitude of this bias error, we speculate that it is opposite in sign and larger in

magnitude than the infrared bias error but less than the latent heat bias error. When adiabatic vertical velocities and the $\omega\alpha$ integral are used to estimate energy conversions, we would emphasize Jensen's statement "that the occurrence of very intense energy transformations within the boundary region is questionable in view of certain non-geostrophic and nonadiabatic effects."

Wiin-Nielsen (1964), using Jensen's (1961) calculations of the adiabatic conversion of available potential energy to kinetic energy for individual layers, estimated that for the northern hemisphere the conversion due to adiabatic motions amounted to 4.24 watts m^{-2} during January, 1958, and 2.71 watts m^{-2} during April, 1958. Our crude estimates of the vertical motion bias errors produced by diabatic effects indicate that these energy conversion estimates should be increased. With an increase they may possibly compare more favorably with Kung's (1966) estimation of 6.4 watts m^{-2} for frictional dissipation and Dutton's and Johnson's (1966) estimate of 5.8 watts m^{-2} for the generation of zonal available potential energy. Admittedly our comment concerning the bias errors due to neglect of diabatic processes are quite speculative; however, our results for the infrared processes, and Danard's for latent heating, and the questionable effects of sensible heating indicate that additional investigations of the energy conversion processes should be undertaken. It is quite possible that the use of adiabatic vertical motions in estimating the energy conversions on a hemispheric scale produce estimates which may be significantly low.

6. CONCLUSIONS

Although the adiabatic method is widely used to estimate large-scale vertical motion and is probably as effective as any of the other commonly used methods, the results of this study indicate that its limitations are considerable. If data from small intervals of pressure are used (e.g. 50 mb) to obtain profiles of adiabatic vertical velocities, it appears that some type of filtering technique such as that used here should be employed to reduce the random errors. In general, considerable variations exist between individual adiabatic profiles, even when the data are filtered and classified according to the amount of cloudiness.

Although in individual cases the infrared contribution to the total vertical motion tends to be quite small, the contribution is quite consistent from one case to another. Thus when mean profiles of adiabatic and infrared velocities are prepared, the contribution of infrared processes appear quite significant, perhaps amounting to 30 percent

of the adiabatic contribution. At night in regions of clear skies the infrared contribution to the downward motion is about 60 to 70 percent of that due to adiabatic motion. In cloudy regions the infrared contribution is practically zero below the cloud, while above the clouds it is just slightly positive. In the presence of a cloud layer the infrared radiation process undoubtedly plays an important role by reducing the hydrostatic stability within the cloud layer and thus increasing the vertical transfer of heat.

Other diabatic processes also reduce the reliability of adiabatic estimates of the vertical motion. The release of latent heat within a cloud and the evaporation of falling rain beneath a cloud are especially important processes. Since, in general, infrared radiation processes along with the absorption of solar energy and release of latent heat are associated with upward motion of air in the warm regions to the east of a growing middle latitude disturbance and the downward motion in the clearer and colder region to the west, the net effect of these diabatic processes should be considered. It appears that in a growing disturbance the diabatic contribution to the vertical motion field may be sufficient to result in a substantially larger energy conversion than that obtained in studies which are based only on adiabatic motions.

REFERENCES

Danard, M. B., 1964: On the influence of released latent heat on cyclone development. J. Appl. Meteor., Vol. 3, No. 1, pp. 27-37.

Dutton, J. A., and D. R. Johnson, 1966: The theory of available potential energy and a variational approach to atmospheric energetics. Advances in Geophysics (accepted for publication), Vol. 12.

Haltiner, G. J., and F. L. Martin, 1957: Dynamical and physical meteorology, McGraw-Hill Book Company, Inc., New York, pp. 316-318.

Hansen, J., and A. H. Thompson, 1965: Vertical motion calculations and satellite cloud observations over the western and central United States. J. of Appl. Meteor., Vol. 4, No. 1, pp. 18-30.

Hildebrand, F. B., 1956: Introduction to Numerical Analysis, McGraw-Hill Book Company, Inc., New York.

Jensen, C. E., 1961: Energy transformations and vertical flux processes over the northern hemisphere. J. Geophys. Res. 66, 4, pp. 1145-1156.

Johnson, D. R., 1965: The role of terrestrial radiation in the generation of available potential energy. Ph. D. thesis, University of Wisconsin, 1965.

Kung, E. C., 1964: Kinetic energy generation and dissipation in the large-scale atmospheric circulation. Monthly Weather Review, Vol. 94, No. 2, pp. 67-82.

Kuhn, P. M., 1966: Personal Communication.

Kuhn, P. M., and D. R. Johnson, 1966: Improved radiometersonde observations of atmospheric infrared irradiance. J. of Geophysical Res., Vol. 71, No. 2, pp. 367-373.

Lorenz, E. N., 1955: Available potential energy and the maintenance of the general circulation. Tellus, Vol. 7, pp. 157-167.

Möller, F., 1951: Thermodynamics of clouds, Compendium of Meteorology, American Meteor. Soc., Boston, 1951, pp. 199-206.

Panofsky, H. A., 1951: Large-scale vertical velocity and divergence, Compendium of Meteorology, American Meteor. Soc., Boston, 1951, pp. 639-646.

Shenk, W. E., 1963: TIROS II window radiation and large-scale vertical motion. J. Appl. Meteor., 2, 6, pp. 770-775.

Starr, V. P., 1958: What constitutes our new outlook on the general circulation. Jour. of the Meteorological Soc. of Japan, series II, Vol. 36, No. 5, pp. 167-173.

Suomi, V. E. and P. M. Kuhn, 1958: An economical net radiometer. Tellus, Vol. 10, pp. 160-163.

White, R. M., and G. F. Nolan, 1960: A preliminary study of the potential to kinetic energy conversions in the stratosphere. Tellus, 12, pp. 145-148.

Wiin-Nielsen, A., 1964: On energy conversion calculations. Monthly Weather Review, 92, 4, pp. 161-167.

List of Symbols

$\frac{dh}{dt}$ = rate of heat addition per unit mass

c_p = specific heat at constant pressure

α = specific volume

R_d = gas constant for dry air

p = pressure

θ = potential temperature

$\omega = \frac{dp}{dt}$ = vertical velocity in pressure coordinates

$\vec{v}_h$ = horizontal wind velocity

g = acceleration of gravity

F_n = net infrared radiation

f = coriolis parameter

u = eastward component of the wind

v = northward component of the wind